HHS Public Access

Author manuscript

Mol Cell. Author manuscript; available in PMC 2020 February 21.

Published in final edited form as:

Mol Cell. 2019 February 21; 73(4): 775–787.e10. doi:10.1016/j.molcel.2018.11.034.

The RNA-binding protein PUM2 impairs mitochondrial dynamics and mitophagy during aging

Davide D'Amico[1], **Adrienne Mottis**[1], **Francesca Potenza**[1], **Vincenzo Sorrentino**[1], **Hao Li**[1], **Mario Romani**[1], **Vera Lemos**[2], **Kristina Schoonjans**[2], **Nicola Zamboni**[3], **Graham Knott**[4], **Bernard L. Schneider**[5], and **Johan Auwerx**[1,6,*]

[1]Laboratory for Integrative and Systems Physiology, Institute of Bioengineering, Ecole Polytechnique Fédérale de Lausanne (EPFL), CH-1015 Lausanne, Switzerland; [2]Laboratory of Metabolic Signaling, Institute of Bioengineering, Ecole Polytechnique Fédérale de Lausanne, CH-1015, Lausanne, Switzerland; [3]Department of Biology, Institute of Molecular Systems Biology, Eidgenössische Technische Hochschule Zürich (ETHZ), CH-8093, Zurich, Switzerland; [4]BioEM Facility, Faculty of Life Sciences Ecole Polytechnique Fédérale de Lausanne (EPFL), CH-1015 Lausanne, Switzerland; [5]Brain Mind Insitute, Ecole Polytechnique Fédérale de Lausanne (EPFL), CH-1015 Lausanne, Switzerland. [6]Lead contact.

Summary

Little information is available about how post-transcriptional mechanisms regulate the aging process. Here, we show that the RNA-binding protein Pumilio2 (PUM2), which is a translation repressor, is induced upon aging and acts as a negative regulator of lifespan and mitochondrial homeostasis. Multi-omics and cross-species analyses of PUM2 function show that it inhibits the translation of the mRNA encoding for the mitochondrial fission factor (*Mff*), thereby impairing mitochondrial fission and mitophagy. This mechanism is conserved in *C. elegans* by the PUM2 orthologue, PUF-8. *puf-8* knock-down in old nematodes and *Pum2* CRISPR/Cas9-mediated knockout in the muscles of elderly mice enhances mitochondrial fission and mitophagy in both models, hence improving mitochondrial quality control and tissue homeostasis. Our data reveal how a PUM2-mediated layer of post-transcriptional regulation links altered *Mff* translation to mitochondrial dynamics and mitophagy, thereby mediating age-related mitochondrial dysfunctions.

Graphical Abstract

*Correspondence to Johan Auwerx at admin.auwerx@epfl.ch.

Author Contributions

D.D. and J.A. conceived and designed the project. D.D and F.P. performed the experiments. A.M., V.S. and M.R. independently replicated worm experiments. V.L. and K.S. designed and performed the *ex vivo* mitochondrial respiration assay. H.L. performed the GSEA. N.Z. measured the metabolome. G.K. performed electron microscopy experiments. B.S. performed the AAV production and contributed to experimental design. D.D. and J.A. wrote the manuscript.

Data and Software Availability

The RNA-seq has been deposited in the GEO repository under ID code GSE121535.

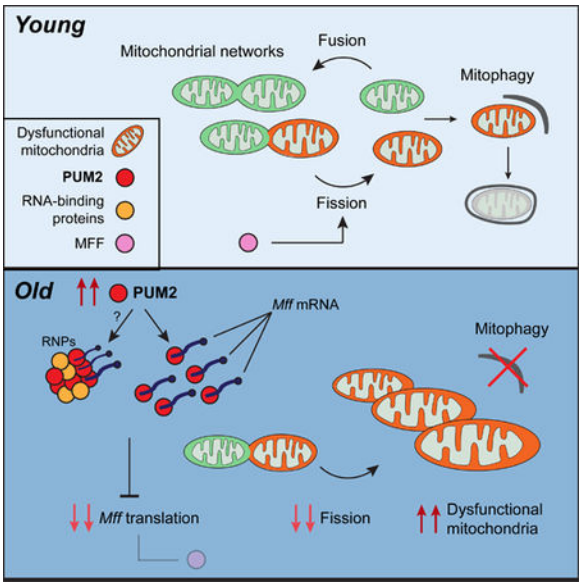

eTOC Blurb

Aging leads to alterations in several key biological processes. However, if and how these age-associated dysfunctions are interconnected is still poorly understood. Here, D'Amico et al., discovered that the RNA-binding protein PUM2 is induced upon aging and links impaired protein homeostasis and mitochondrial dysfunction, two well-known hallmarks of aging.

Introduction

Aging is characterized by a functional decline in most biological processes including alterations in cellular (Houtkooper et al., 2010) and mitochondrial metabolism (Sun et al., 2016). Despite the wealth of data available on the transcriptional control of the aging process across different species, the involvement of post-transcriptional regulatory mechanisms is much less studied. Among such processes, regulation of protein synthesis and degradation, which assures proteostasis, is emerging as a key process in aging (Gonskikh and Polacek, 2017; Steffen and Dillin, 2016). RNA-binding proteins (RBPs) are interesting within this context, as they bind ribonucleic-acid molecules regulating their fate after transcription (Shi and Barna, 2015). RBPs contain low-complexity (LC) domains that mediate their condensation in ribonucleoprotein (RNP) granules, which exert a role in mRNA translation, metabolism and transport (Sheinberger and Shav-Tal, 2017). These structures also mediate the response to cellular stress, by assembling RBPs and their target mRNAs in stress granules (SGs), where protein translation is repressed (Sheinberger and Shav-Tal, 2017). The abnormal function of RBPs is the cause of several neuromuscular degenerative disorders (Huang et al., 2010; Harrison and Shorter, 2017). A few relevant examples include the RBPs FUS and TDP-43, in the context of amyotrophic lateral sclerosis (ALS), and frontotemporal lobar degeneration with ubiquitin-positive inclusions (FTLD-U) (Gitler and Shorter, 2011); PABPN1 in the oculopharyngeal muscular dystrophy (OPMD) (Banerjee et al., 2013), and TIA1 in Tau-dependent Alzheimer's disease (Apicco et al., 2018) and in distal myopathies (Lee et al., 2018). The mechanisms by which RBPs cause these pathologies are disease-

specific. However, a common effect of pathogenic RBPs is a profound alteration of cellular proteostasis, as they lead to the abnormal accumulation and aggregation of RNP granules. In addition, they can impair protein homeostasis at the level of protein synthesis, by affecting the translational efficacy of their target mRNAs.

While the role of RBPs is getting unveiled in the setting of diseases, only a few RBPs have been investigated in the context of aging, and the mechanisms underpinning their function in aging are not well characterized (Chaturvedi et al., 2015; Masuda et al., 2009). Towards this end, we systematically screened for RBPs that are altered upon aging of muscle and brain, the tissues in which this class of proteins is most frequently associated with diseases. This led us to identify the RBP, PUM2, as a negative regulator of longevity and healthspan in nematode and mouse models. We furthermore identify the mitochondrial fission factor (*Mff*) as a novel PUM2 mRNA target. PUM2-mediated translational inhibition of *Mff* leads to aberrant mitochondrial dynamics and, as consequence, reduces mitophagy and mitochondrial function. Therefore, PUM2, alone or as part of RNP complexes, represents a driver of a novel post-transcriptional mechanism that could link altered proteostasis to mitochondrial dysfunction during aging.

Results

PUM2 is a negative regulator of lifespan.

We analysed the expression of the repertoire of known mammalian RBPs (Neelamraju et al., 2015) in extant transcriptome data from aged mouse muscle tissues (Edwards et al., 2007) (Figure S1A) and found that only the expression of 66 out of 1343 RBPs was significantly changed in both young *vs*. old and old *vs*. old calorie restricted (CR) muscle samples (Figure S1B). *Pumilio2* (*Pum2*) showed a robust increase upon aging, which was restored to the level of young mice in aged CR muscles (Figures S1B and C). *Pum2*, *Rbm6* and *Nudt16l* are furthermore the only three RBP transcripts that are commonly regulated between three datasets (Figure 1A), *i.e*. aged mouse muscle (Edwards et al., 2007) (Figure S1C), neocortex of aged mice (Oberdoerffer et al., 2008) (Figure S1D and E), and muscle biopsies of aged humans (Yang et al., 2015). Among these three candidates, *PUM2* is the only transcript whose levels are consistently up-regulated upon aging in a skeletal muscle compendium of gene expression in human biopsies (Su et al., 2015). We confirmed the increase of PUM2 expression also at the protein level in quadriceps (Figure 1B), forelimb (Figure 1C) and tibialis (Figure S1F) muscles of aged C57BL/6J mice. PUM2 levels were also increased in the neocortex of old mice (Figure S1G). Of importance, *Pum2* levels in neocortex and whole brain were inversely correlated to mean longevity, in the BXD (Gelman et al., 1988) and in the LXS (Liao et al., 2010) mouse genetic reference populations (Figure 1D), suggesting a negative effect of the increase of PUM2 on the aging process.

To experimentally validate this suggestive effect on lifespan, we used the short-lived nematode *Caenorhabditis elegans*. Phylogenetic analysis indicated that *puf-8* was the closest orthologue of mammalian *Pum2* (Spassov and Jurecic, 2003). In wild-type Bristol N2 worms, *puf-8* transcript levels gradually increased upon aging (Figure S1H), consistent with the observations in mice and humans. *puf-8* loss-of-function (LOF) affects germline maturation and worm development (Subramaniam and Seydoux, 2003). To avoid these

pleiotropic effects, we used germline deficient *glp-1(e2144)* mutant worms to test *puf-8* impact on lifespan. Consistent with the prior literature, *glp-1* lived longer compared to N2 worms (Figure S1I) (Arantes-Oliveira et al., 2002). Importantly, in *glp-1* mutants, *puf-8* levels increased in an age-dependent manner (Figure 1E), and *puf-8* LOF improved lifespan (Figure 1F), an effect accompanied by a significant increase in fitness of the old worms (Figure S1J). Thus, these results suggest that the age-dependent increase of both *Pum2* and of its *C. elegans* orthologue, *puf-8*, could contribute to accelerate the aging process.

PUM2 is a negative regulator of mitochondrial function

PUM2 mainly acts as a repressor of protein synthesis, by binding and inhibiting the translation of mRNAs containing the 5′-UGUAXAUA-3′ Pumilio-binding element (PBE) (Hafner et al., 2010) and it was linked to germ-cell development (Fox et al., 2005), genome stability (Lee et al., 2016) and synaptic morphogenesis (Vessey et al., 2010). Moreover, PUM2 harbours LC regions that upon stress, allow it to form stress granules, in which its target mRNAs are trapped and unable to be translated (Vessey et al., 2010). To further understand PUM2's biological role, we performed a multi-tissue GSEA (gene set enrichment analysis) in the human GTEx cohort (GTEx Consortium, 2013). As expected, *PUM2* transcript levels positively correlate with genes in the gene ontology (GO) categories to which PUM2 belongs, such as "Cytoplasmic stress granule" and "Regulation of post-transcriptional gene silencing" (Figure S2A). Strikingly, all the top 15 GO categories negatively correlating with *PUM2* are linked to mitochondrial function (Figure S2A), except the category "Ribosomal subunits", which could be, however, in line with PUM2's role as a translation repressor. Tissue-specific GSEA, confirmed that PUM2 positively correlates with stress granules genes and inversely correlates with mitochondrial genes, in both human brain cortex (Figure 1G and H and Figure S2B) and cerebellum (Figure S2C and D). Consistently, the loss of function of *puf-8* and *Pum2* improves both basal and maximal respiration in old worms (Figure 1I) and in mouse myoblasts (Figure 1J and S2E), respectively. Thus, these results suggest that the accumulation of both PUM2 and PUF-8 could accelerate the aging process by impairing mitochondrial function.

Multi-omics analyses reveal MFF as a novel post-transcriptional target of PUM2

Previous studies on PUM2 function in mammals were mainly based on either transcriptomic or ribonomic analyses (Bohn et al., 2017; Hafner et al., 2010; Lee et al., 2016), inciting us to apply a multi-omics approach to reveal post-transcriptional effects of PUM2 that could link it to mitochondrial function. First, we performed quantitative proteomics after stable isotope labelling with amino acids (SILAC) in HeLa cells. We identified 4485 proteins, of which 85 are commonly up-regulated and 58 down-regulated, in *PUM2* knock-down (*PUM2*sh) versus control (SCR) cells (Figure 2A, red dots). The higher number of induced *vs.* repressed proteins is consistent with the removal of PUM2 as a translation inhibitor. The network of induced targets showed a tight functional interaction (Figure 2B) and was significantly enriched for metabolic pathways (Figure 2C). In line with the GSEA, the cellular component enrichment analysis suggests that these changes could be driven by mitochondrial-dependent mechanisms (Figure 2D). Also untargeted metabolomics of *PUM2*sh *vs.* control cells showed that mitochondrial and metabolic pathways, such as TCA cycle and purine/pyrimidine pathways were among the top hits (Figures 2E, S3A and B).

We then performed RNA-Seq to discriminate between transcriptional and post-transcriptional responses driven by *PUM2* depletion and the multi-layered analysis showed only 36 candidates upregulated at protein, but not at mRNA level (Figure 2F, S3C and S3D). Finally, to identify the direct PUM2 targets leading to these changes, we crossed the proteins from the multi-omics analysis with the list of client transcripts bound by PUM2 in human CLIP-Seq data (Hafner et al., 2010). Nine candidates are both bound and repressed by PUM2 and only two of them have a perfect PBE in their 3'UTR (Figure 2G) and include mitochondrial fission factor (MFF), an outer mitochondrial membrane (OMM) protein required for mitochondrial fission by recruiting the dynamin-like protein DRP1 (encoded by the gene *DNML1*) (Otera et al., 2010) and SLC6A6, a plasma membrane taurine-alanine transporter, whose up-regulation is in line with the increase of taurine and alanine in *PUM2*sh cells (Figure S3E). MFF contains the most highly conserved PBE in different species, including in the *C. elegans* MFF orthologue, *mff-1* (Figure 2H). This evidence, together with its direct role in mitochondrial function, pinpoints MFF as a potential mediator of PUM2's effects on mitochondrial homeostasis.

PUM2 regulates mitochondrial dynamics via MFF

We validated whether PUM2 negatively regulates MFF, using two independent shRNAs in mouse C2C12 myoblasts and human HeLa cells. *Pum2* depletion increased MFF at the protein (Figure 3A and 3B, Figure S4A), but not transcript levels (Figure 3C and Figure S4B to S4C) in mouse C2C12 and human HeLa cells, supporting its role in post-transcriptional regulation. *Mff* has a stable 3'UTR, a feature of post-translationally regulated mRNAs (Figure S4D). Cross-linking and immunoprecipitation (CLIP)-qPCR of PUM2 demonstrated its binding to the *Mff*, but not *Actb*, 3'UTR (Figure 3D and Figure S4E) and *Pum2* depletion in C2C12 cells increased the luciferase activity of a reporter construct under the control of *Mff* 3′UTR sequence (Figure 3E). To establish a causal link between PUM2 and MFF, we generated C2C12 cells with a genomic deletion of a *Mff* 3'UTR region that contains the PUM-binding element (ΔPBE-*Mff* cells), using CRISPR (Figure S4F and S4G). ΔPBE-*Mff* C2C12 cells have higher levels of MFF, in line with the fact that *Mff* mRNA cannot be bound and repressed by PUM2. Moreover, *Pum2* silencing was unable to further enhance MFF levels (Figure 3F). Altogether, these data demonstrate that PUM2 binds and specifically represses the translation of *Mff* mRNA.

Consistent with the age-dependent increase of PUM2 (Figure 1A to C), MFF levels are reduced upon aging (Figure S4H) in mouse gastrocnemius. On the other hand, the mitochondrial fission activator, DRP1, is induced in the same context (Figure S4H), suggesting possible compensatory effects to rescue the age-related reduction in mitochondrial fission. Interestingly, the levels of SLC6A6, the other PUM2 target identified by our multi-omics screening, was increased in tissues from old versus young animals (Figure S4H), excluding a major role of the PUM2/SLC6A6 axis in the setting of aging.

Increased MFF levels are reported to cause a shift of mitochondrial dynamics towards fission (Otera et al., 2010). In line with this premise, PUM2 depletion increased the percentage of myoblast cells undergoing fission (Figure 3G and Figure S4I). This effect is MFF-dependent, since the double knock-down of both *Pum2* and *Mff* restores mitochondrial

morphology to the basal state (Figure 3G and S4I). In addition, in DPBE-*Mff* C2C12 cells basal mitochondrial fission was not further enhanced after *Pum2* knock-down (Figure 3H and S4J). Importantly, PUM2 depletion specifically affects mitochondrial, but not peroxisome morphology, as assessed by the staining of SCR and *Pum2*sh C2C12 cells with the mitochondrial protein, CRIF1, and the peroxisome marker, Catalase (Figure S4K).

PUM2 regulates mitophagy via MFF

Increased fission is accompanied by improved removal of fragmented mitochondria through mitophagy (Frank et al., 2012; Tanaka et al., 2010; Twig et al., 2008). We tested whether *Pum2*sh C2C12 cells showed an increase in mitophagy rates, using the mitophagy marker m-KEIMA (Katayama et al., 2011). When mitochondria are at neutral pH, m-KEIMA is excited at 440 nm (pseudocolored in cyan), whereas in mitochondria undergoing mitophagy changes its excitation wavelength (represented in red). Indeed, C2C12 *Pum2*sh clones exhibited increased mitophagy rates compared to control cells (Figures 4A and 4B). Consistently, mitochondrial to nuclear DNA ratio (mtDNA/nDNA) was lower in *Pum2*sh clones (Figure S5A).

To assess the mechanism by which reduced PUM2/increased MFF triggered mitophagy, we characterized the involvement of both PINK1/Parkin-dependent and -independent mechanisms in isolated mitochondrial fractions of control and *Pum2*sh C2C12 cells. Depletion of *Pum2* led to the accumulation of mitochondrial Parkin, phosho-S65 Ubiquitin and Optineurin, supporting a role of Parkin-dependent mitophagy (Figure 4C). In addition, *Pum2*sh clones showed a striking increase of BNIP3 (Figure 4C), an OMM receptor that mediates Parkin-independent mitophagy (Palikaras et al., 2018). These data suggest that inducing MFF, by silencing *Pum2*, enhances mitophagy in mouse myoblasts. Indeed, *Mff* RNAi (Figure S5B) repressed *Pum2*sh-mediated mitophagy (Figure S5C and S5D) and a mild overexpression of MFF (Figure S5E) induced mitophagy in C2C12 cells (Figure 4D and 4E). Finally, ΔPBE-*Mff* cells exhibited an increased basal mitophagy, independently on *Pum2*sh (Figure S5F and S5G). In line with this data, *MFF* mRNA levels of human muscle biopsies from the GTEx dataset positively correlated with the expression of mitophagy genes (Figure 4F), the highest correlation being with *SQSTM1*, *BNIP3*, *BNIP3L* and *PARK7* (Figure 4G). Our data hence link PUM2 to mitochondrial autophagy via MFF, and suggest that the increase of PUM2 that we observed upon aging could impair mitochondrial dynamics and mitophagy, both hallmarks of aging (Sun et al., 2016).

puf-8 depletion improves mitochondrial homeostasis during nematode aging

Aging is accompanied by the accumulation of giant, dysfunctional mitochondria, that cannot be eliminated by mitophagy, as reported in muscles of nematodes (Yasuda et al., 2006), flies (Rana et al., 2017) and mice (Leduc-Gaudet et al., 2015). We confirmed the increase of swollen mitochondria in old (Day 8) relative to young (Day 1) worms that express $p_{myo\text{-}3}$::mito::GFP, a GFP localized in the mitochondria of body wall muscles (Figure S6A). Importantly, *puf-8* RNAi feeding from the adult stage reverted this aging phenotype (Day 8, *puf-8*) and re-established mitochondrial networks similar to those of young worms (Figure 5A). In addition, double RNAi of both *puf-8* and *mff-1* cancelled the normalizing effect of *puf-8* LOF on mitochondrial morphology (Figure 5A). *puf-8* depletion also increased the

expression of the mitophagy markers *dct-1* and *pink-1* (Figure 5B), the worm orthologues of *Bnip3* and *Pink1*, and of several OXPHOS genes (Figure S6B), in a *mff-1*-dependent fashion. Interestingly, no changes were observed in markers of mitochondrial and endoplasmic reticulum unfolded protein response (UPR^{mt} and UPR^{er}, respectively) and heat shock response (HSR) (Figure S6C) and in peroxisome morphology of old worms (Figure S6D), supporting a specific role of *puf-8* in mitochondrial dynamics and mitophagy.

To validate the effect of *puf-8* on mitophagy we quantified the mitochondrial mass of muscles of young and old p_{myo-3}::mito::GFP worms, as previously described (Palikaras et al., 2015). *puf-8* RNAi alone reduced the intensity of the mitochondrial-localized GFP (Figure 5C and 5D), with no differences between *puf-8* and *puf-8/dct-1* worms, and decreased the mtDNA/nDNA ratio (Figure 5E), in a *dct-1* dependent manner, of young adult worms (Day 5). This observation was in line with the model by which *puf-8* represses mitophagy. On the other hand, in older worms (Day 8), *puf-8* depletion increased both mitochondrial mass (Figure 5F and 5G) and mitochondrial DNA content (Figure 5H), an effect lost in *puf-8*/*dct-1* RNAi nematodes. This is consistent with previous literature showing that long-term boosting of mitophagy is followed by activation of mitochondrial biogenesis (Palikaras et al., 2015; Ryu et al., 2016). These data are also in agreement with the increased citrate synthase activity of old worms exposed to *puf-8* RNAi, an effect that is reduced in *puf-8*/*dct-1* worms (Figure S6E). Importantly, the effects of *puf-8* on mitochondria also impact on the general muscle homeostasis, since *puf-8* worms showed reduced aging-related muscle fiber damage in both an *mff-1* (Figure 5I) and *dct-1* (Figure S6F) dependent fashion. Finally, the increased longevity of *puf-8* RNAi worms was largely blunted by the combined *puf-8/mff-1* RNAi (Figure 5J), while *mff-1* RNAi alone led to a mild, but not significant, increase of the nematode's lifespan. These data demonstrate an evolutionary conserved role of PUM2 and show that *puf-8* negatively regulates *C. elegans* longevity by contributing to aging-dependent alterations in mitochondrial dynamics and mitophagy.

PUM2 knock-down in old mice improves mitochondrial function

To ascertain whether PUM2 inhibition affects mitochondrial dynamics and quality also during mammalian aging, we knocked-down *Pum2* in muscles of old mice *in vivo* using the CRISPR-Cas9 system (Ran et al., 2015). First, we tested three different *PUM2*-targeting guides (*gPUM2*) in HEK293T cells and selected the guide leading to the most efficient knock-down of *PUM2* and consequent upregulation of its target, MFF (g*PUM2* #1, Figure S7A). Sequencing of the region around the gRNA-targeted site confirmed the efficient genome editing of *PUM2* gene (Figures S7B). We then injected Cas9/*gPum2* or Cas9 (as a control) encoding AAV9s, bilaterally, in gastrocnemius muscles of 23-months-old C57BL/6J mice. *Pum2* depletion in the muscle of old mice increased the MFF protein (Figure 6A), but not mRNA level (Figure S7C) and induced the fragmentation (Figure 6B) and reduction in volume fraction (Figure 6C and D and Movies S1 and S2) of hyperfused and swollen intermyofibrillar (IFM).

Consistent with the data in cells and worms, LOF of PUM2 also affects mitophagy *in vivo*. Indeed, depletion of *Pum2* induced mitochondrial BNIP3 (Figure 6E). However, differently

to what shown in C2C12 cells (Figure 4C), no changes in phospho-S65 ubiquitin were observed (Figure 6E), in mouse muscle. Similar to nematodes, *Pum2* knock-down in the gastrocnemius increased citrate synthase activity (Figure 6F) and the levels of a subset of OXPHOS proteins (Figure 6G). High-resolution respirometry analysis confirmed that g*Pum2* muscles of old mice had better CII-driven and $State_{3ADP}$ (CI + CII) mitochondrial respiration, compared to controls (Figure 6H). Altogether, the CRISPR-Cas9 genome editing of *Pum2* in the muscle of elderly mice shows that PUM2 regulates mitochondrial dynamics and function, as well as mitochondrial clearance upon aging.

PUM2 interacts with *Mff* mRNA and other RBPs in aged-tissues

Endogenous PUM2 binds *Mff* in mice brain extracts and this interaction is strikingly higher in old compared to young animals (Figure 7A). This indicates that PUM2 could exert its role on mitochondrial homeostasis, in aged tissues, by binding and repressing the translation of *Mff* mRNA, similarly to what was observed in cells (Figure 3D). To further study the mechanism of action of PUM2 during aging, we immunoprecipitated endogenous PUM2 from young and old mouse brains and performed liquid chromatography–mass spectrometry ($LC\text{-}MS^2$) to analyse the PUM2 interactomes. We filtered the proteins interacting with PUM2 in old but not young tissues (Figure 7B) and pathway enrichment analysis indicated that several of the aging-associated PUM2-binding proteins belonged to categories related to microtubule organization (Figure 7C and S7D) and the Molecular Function category "RNA-binding proteins" (Figure 7C). Many of these proteins were regulators of protein translation and components of the deadenylase and RNA-helicase complexes, including known PUM2-binding partners, such as CNOT1 (Etten et al., 2012), members of the eIF4F complex and PABP (Padmanabhan and Richter, 2006; Vessey et al., 2010) (Table S4). The candidates PABPC and eIF3A, were further validated by CoIP-immunoblot analysis (Figure 7D). These observations raised the possibility that PUM2 functions as part of larger RNP complexes. Indeed, when certain RBPs are highly concentrated they spontaneously tend to form larger and more stable aggregates (Molliex et al., 2015). In line with this, a GFP-tagged PUM2 protein expressed at low levels mostly exhibited a punctate distribution in the cytosol, while increasing the expression of GFPPUM2 dose-dependently resulted in more and bigger condensates that co-localized with the endogenous RBP PABPC (Figure S7E to S7G). Since PUM2 protein levels are induced upon aging, we speculated that this could enhance the formation of RNPs *in vivo*. To verify this hypothesis, we isolated both cytosolic and RNP fractions from young and old mouse brains, adapting a protocol developed in (Wheeler et al., 2017), and showed that PUM2 increased upon aging in both cytosol and RNP pellets. Moreover, PUM2 cofractionated in RNP complexes together with other RBPs identified in the interactome analysis, such as PABPC, eIF3A and STAU1 (Figures 7E and Figure S7H). Furthermore, PUM2 co-localized with Thioflavin S (ThS), a dye which stains amyloidogenic aggregates (Molliex et al., 2015), in mouse neocortex tissues (Figure S7I), and the size (Figure S7J) and number (Figure S7K) of the PUM2 granules was significantly increased when comparing young to old animals. Altogether, these data show that PUM2 accumulates in aged tissues and binds more *Mff* mRNA. PUM2 could exert this function alone or as part of RNP aggregates. The PUM2-dependent repression of *Mff* translation leads to impaired mitochondrial fission, mitophagy and ultimately to age-associated mitochondrial dysfunction (Figure 7F).

Discussion

The post-transcriptional control of the aging process has been poorly studied so far. Here, we show how the RNA-binding protein, PUM2, affects the translation of specific mRNAs, such as *Mff*, in old animals with consequences on cellular metabolism and organismal physiology.

Our multi-omics analyses identified the mitochondrial fission factor, *Mff*, which recruits DRP1 to the mitochondria, as a novel PUM2 mRNA client. Reduced fission/increased fusion rates have already been associated with accumulation of hyperfused mitochondria in aged tissues (Yasuda et al., 2006; Rana et al., 2017; Leduc-Gaudet et al., 2015). Here, we propose that the PUM2-mediated repression of *Mff* translation and the consequent deficit in mitochondrial fission and mitophagy contributes to the imbalance in mitochondrial dynamics observed upon aging. Indeed, the respective LOF of *puf-8* and *Pum2*, in old worms and mice, increases fission and mitophagy and rescues the age-associated abnormal mitochondrial networks (Rana et al., 2013; Sun et al., 2016), in an *mff-1/Mff*-dependent manner.

In particular, we show that PUM2/MFF regulates both Parkin-dependent and independent mitophagy in myoblast cells, whereas it acts mainly through the receptor DCT-1/BNIP3 in old worms and mice. Although the exact mechanism by which PUM2 regulates mitophagy, *in vitro* and *in vivo*, is still elusive and an interesting subject for future studies, our data support the concept that mitochondrial fission induces the selective removal of dysfunctional mitochondria (Kageyama et al., 2014; Rana et al., 2017). This model is apparently in contrast with previous studies reporting that high levels of MFF inhibit mitophagy (Yamashita et al., 2016) and that loss of mitochondrial fission enhances mitophagy (Burman et al., 2017). However, these studies evaluated the role of MFF in the context of mitophagy induced by mitochondrial toxins and stressors in HeLa cells. In our study, however, the absence of stressors combined with the mild and probably more physiologically relevant changes of MFF levels could explain why MFF induces mitophagy in C2C12, as opposed to its inhibitory action observed in HeLa cells. In addition, *Mff* loss-of-function was shown to reduce mitophagy in (Chen et al., 2015). However, these phenotypes were measured only in young animals and both our and previous studies (Rana et al., 2017) show that the induction of mitochondrial dynamics in old animals is correlated to increased mitophagy, mitochondrial function and longevity. Finally, although MFF also plays a role in peroxisome morphology (Gandre-Babbe and van der Bliek, 2008), we demonstrate that the PUM2/MFF axis did not affect these organelles and hence mediates its effect on lifespan and healthspan through an impact on the mitochondria.

As regards how PUM2 mechanistically acts on MFF, the simplest model is that PUM2 expression increases upon aging, binds more *Mff* mRNA and leads to mitochondrial defects. However, we also show that PUM2 binds several RBPs and components of the translational machinery, specifically in tissues of old animals. Therefore, an intriguing hypothesis is that, upon aging, PUM2 could exert its role of repressor also as part of larger RNP structures. Indeed, the accumulation and detrimental function of RBP-containing RNPs in aging has been already described in yeast (Schlissel et al., 2017) and in *C. elegans* (Lechler et al.,

2017) and our data seem to suggest that these structures may be conserved also in mammals. It is furthermore tempting to speculate that the PUM2-containing RNPs could share similarities with those that are causally linked to neuromuscular degenerative disorders, such as ALS and tauopathies (Harrison and Shorter, 2017; Maziuk et al., 2018). Further studies are, however, required to understand the exact mechanism of how PUM2 represses *Mff* mRNA---either acting alone, in the context of RNPs or through a combination of both---in aging.

In conclusion, our work demonstrates that the RBP PUM2 inhibits *Mff* mRNA translation, thereby deregulating mitochondrial dynamics and mitophagy in old animals. PUM2 hence controls both proteostasis and mitochondrial function, two converging pathways that are impaired during aging. Reducing PUM2 levels or activity, either genetically or pharmacologically, may hence restore cellular homeostasis during the aging process.

STAR★Methods

Contact for Reagent and Resource Sharing

Further information and requests for reagents may be directed to, and will be fulfilled by the corresponding author Johan Auwerx (admin.auwerx@epfl.ch).

Experimental Model and Subject Details

Mice—24 months old male C57BL/6J mice (Janvier) were bilaterally injected in the gastrocnemius muscles with $5*10^{11}$ viral particles containing the g*Pum2*#1 (left leg) or the p×601 vector as control (right leg) (n = 7). Mice were housed single-caged. After 5 weeks, animals were randomized, sacrificed and processed to perform electron microscopy imaging (n = 2 per condition) and for all biochemical and functional analyses described below (n = 5 per condition). For the latter analyses, gastrocnemius muscles were rapidly removed and snap-frozen in liquid nitrogen. 2 months and 24 months old male C57BL/6J mice (Janvier) (n = 3) were sacrificed and whole brain and tibilialis anterioris tissues were OCT-embedded for immunohistochemical analysis, while quadriceps and forelimb muscles were rapidly snap-frozen. No blinding was used during the experiment procedures. All experiments were performed in compliance with all relevant ethical regulations. The mice experiments were authorized by the local animal experimentation committee of the Canton de Vaud, under license 2890. The committee that approved the license is the Commission cantonale pour l'expérimentation animale.

Cell cultures—C2C12 myoblasts (female, ECACC, 91031101) were cultured in Dulbecco's modified Eagle's medium with high glucose content (Gibco, DMEM, 41966–029), 20% of Fetal Calf Serum (FCS) and 100U/mL penicillin and 100μg/mL streptomycin (Gibco, 15140–122). HeLa (female, ATCC® CCL-2™), HEK-293T (ATCC® CRL-3216™) and HEK AAV-293 cells (Agilent, 240073) cells were cultured in the same condition described above, but with 10% FCS. HeLa and C2C12 stable clones were cultured as described above with the addition of puromycin 2 μg/ml (Invivogen, QLL-38–03A) as a selection antibiotic. Trypsin-EDTA 0.05% (Gibco, 25300–062) was used for all the cell lines. All cells were maintained at 37°C and 5% CO_2.

C. elegans* Strains and Bacterial Strains—C. elegans* strains were provided by the Caenorhabditis Genetics Center (University of Minnesota). N2 Bristol, SJ4103 (zcIs14[myo-3::GFP(mit)]), VS11 (hjIs73 [vha-6p::GFP::daf-22]) and RW1596 (stEx30 [myo-3p::GFP::myo-3 + rol-6(su1006)]) strains were cultured at 20 °C. The *glp-1*(e2144ts) strain (CF1930) was cultured at 15°C. All strains were cultured on nematode growth media agar plates seeded with *E. coli* strain OP50. To perform the experiments, *glp-1*(e2141ts) eggs were seeded on plates and raised at 25°C (to eliminate germ cells) for ~40 hours, then shifted to 20°C for the rest of life. Bacterial RNAi feeding experiments were carried out as described in (Kamath et al., 2001), from Day 1 of adulthood, unless differently specified. Clones used were puf-8 (C30G12.7), mff-1 (F11C1.2) and dct-1 (C14F5.1). Clones were purchased from Source BioScience and verified by sequencing.

Method details

C. elegans* motility, survival and oxygen-consumption assays—C. elegans* movement analysis was performed as described in (Mouchiroud et al., 2016), starting from day 1 of adulthood, using the Movement Tracker software. The experiments were repeated at least twice. Lifespan tests were performed at 20 °C as described in (Mouchiroud et al., 2013). Worms that crawled off the plate or had an exploded vulva phenotype were censored. These exclusion criteria were established before starting the experiments. Oxygen consumption was measured using the Seahorse XF96 respirometer (Seahorse Bioscience) (Koopman et al., 2016). Maximal respiration was measured after injecting carbonyl cyanide-4(trifluormethoxy)phenylhydrazone (FCCP, C2920, Sigma-Aldrich) at a final concentration of 10 μM in the well. Respiration rates were normalized to the number of worms in each individual well and calculated as averaged values of 6–7 repeated measurements. Each experiment was repeated at least twice.

Cell transfection and transduction—Lentiviruses were produced by cotransfecting HEK293T cells with lentiviral, packaging (pCMV-dR8.2 dvpr, Addgene, #8455) and envelope (pCMV-VSV-G, Addgene, #8454) plasmids, in a ratio of 4:3:1, respectively, by using FuGENE 6 (Promega, E2691) following manufacturer's instructions. Transfection medium was removed 24 h after transfection and fresh medium was added to the plate. Cell supernatants were collected at 24 and 48 h and filtered through a 0.45-μm filter. Cells to be transduced were seeded 24 hours before infection and then transduced with virus-containing supernatant supplemented with 5 mg/ml of polybrene (Millipore). This step was repeated twice and cells were left to recover for 24 h in growth media before puromycin (2 μg/ml) selection. The list of shRNAs are shown in Supplementary Table 5. HEK293T were seeded onto 6-well plates and transfected in with increasing amounts of EGFP-PUM2 (Low = 0.03 μg, High = 1 μg; 0.1 μg and 0.3 μg correspond to the two intermediate conditions, respectively) or with pEGFP C1 (1 μg), as control, for 24 hours and C2C12 were transfected with Flag-MFF of pcDNA3, as control, using FuGENE6. To assess mitophagy, HEK293T were transfected with m-KEIMA (pCHAC-mt-mKeima, Addgene #72342) together with the pCL-Ampho Retrovirus Packaging Vector (Novus Biologicals) in a ratio 1:1, by using FuGENE 6. Cell supernatants were collected at 48 h and filtered through a 0.45-μm sterile filter. C2C12 cells were transduced with the virus-containing supernatant, left to recover for 24 h in growth media and analyzed by confocal imaging. For siRNA transfection in C2C12,

Lipofectamine® RNAiMAX (Thermo Scientific, 13778100) was used following manufacturer's instructions. 50 picomoles of the siRNA listed in Supplementary Table 5 (synthetized by Microsynth, custom made) were transfected and cells were analyzed by confocal imaging after 48 hours.

Western blot analysis—Cells and tissues were lysed in RIPA buffer [50 mM tris (pH 7.4), 150 mM NaCl, 5 mM EDTA, 0,1% SDS, 1% NP40, 100 mM NaF, 5mg/ml Sodium deoxycholate] with Halt™ protease (Thermo Fisher Scientific, 78430) and phosphatase (Thermo Fisher Scientific, 78442) inhibitor cocktails. Mitochondrial fractions were isolated are described in (Ryu et al., 2016). Protein concentration was assessed by DC protein assay (Bio-Rad, 500–0116). Lysates were eluted in 5× Laemmli buffer (715mM β-mercapto-ethanol, 1M Tris-HCl pH 6.8, 30% Glycerol, 10% SDS, 0.25% Blu Bromophenol). Equal amounts of proteins were separated by SDS-PAGE and transferred onto polyvinylidene difluoride membranes (Millipore, Immobilion-P IPIVH00010). Filters were washed in TBS + 0,05% Tween and blocked for 1 hour with 5% Non-Fat milk. For co-immunoprecipitation assays, cells and tissues were lysed in CoIP buffer (50mM Tris-HCl pH 7.4, 75mM NaCl, 1% NP-40, 0,1% SDS, 5mg/ml Sodium deoxycholate. 1ml of CoIP buffer for 20 million of cells, 5ml for one whole brain lysate) plus protease and phosphatase inhibitor cocktails. 1mg of clear supernatants from cells or 2mg from whole brain extracts were precleared with 30μl of Protein A/G Agarose beads (Pierce, 20421), 2μg of rabbit Igg (Santacruz, sc-2027) and 0,05% BSA and incubated 1 hour at 4°C on a rotating wheel. 2.5% of the precleared lysates were used as input. The rest of the precleared extracts were incubated with 5μg of either an antibody against PUM2 (Abcam, ab10361) or of rabbit control IgG (Santacruz, sc-2027) overnight at 4°C on a rotating wheel. Samp les were added with 50μg of Protein A/G Agarose and incubated on the rotating wheel for additional 1 hour. Beads were washed 5 times in CoIP buffer, eluted in 5× Laemmli Buffer and boiled at 95°C. Supernatants were analyzed by western blot as described above. Proteins were detected using the following antibodies: PUM2 (Santacruz, sc-514108, 1:2000, for cell extracts; Abcam, ab10361, 1:2000, for tissue lysates), MFF (ProteinTech Group, 17090–1-AP, 1:1000), OXPHOS cocktail (Mitoscience/Abcam, ab110413, 1:2000), PABPC (Abcam, ab21060, 1:3000), BNIP3 (Cell Signaling, 3769S, 1:1000), Parkin (Cell Signaling, 4211, 1:500), phospho S65-Ubiquitin (Millipore, ABS1513-I, 1:1000), OPTN (ProteinTech, 10837–1-AP, 1:1000), TOM20 (Santacruz, sc-17764, 1:3000), TOM40 (Santacruz, sc-365467, 1:2000), VDAC (Abcam, ab14734, 1:3000), eIF3A (Abcam, ab86146, 1:2000), STAU1 (Abcam, ab73478, 1:2000), DRP1 (Cell Signaling, 14647, 1:1000), SLC6A6/TAUT (Santacruz, sc-166640, 1:1000), GAPDH (Cell Signaling, 2118, 1:3000), HSP90 (BD Transduction Laboratories, 610418, 1:4000). The secondary antibodies used were goat-anti-rabbit (Cambridge Bioscience, AC2114, 1:5000), goat-anti-mouse (Cambridge Bioscience, AC2115, 1:5000), donkey-anti-goat (Cambridge Bioscience, AC2149, 1:2500) and goat-anti-Guinea pig H&L HRP (Abcam, ab6908, 1:2500) HRP secondary antibodies. Antibody reactions detection were imaged using the c300 imaging system (Azure Biosystems). Quantification of the protein band intensity was performed using using the Fiji "Analyze/Gel" function.

Tissue and cell immunofluorescence analysis—Tissue immunostaining was performed on fresh frozen section of mice tibialis anterior muscles and whole brain tissues.

8μm sections were cut from OCT-embedded samples. Sections were fixed with 4% PFA for 20 min, permeabilized in PBS + 0,5% Triton-X-100 and blocked with 3% BSA+ 10% donkey serum for 1 hour at RT. Sections were stained using an antibody against PUM2 (Abcam, ab10361, 1:300) overnight at 4°C and incubated with the secondary antibody (donkey anti-rabbit Alexa 568, 1:1000) 1 hour at RT. A final counterstaining with Hoechst (Thermo Scientific, 33342, 1:10000) was performed for 3 min. ThS staining was performed for 15 minute RT (ThS 0,03% in 50% EtOH), prior primary antibody incubation. C2C12 clones and HEK293T were fixed with 4% PFA for 20 minutes, permeabilized with 0.1% Triton-X-100 and blocked with 3% BSA 1 hour at RT. For mitochondrial morphology analysis, cells were stained with Tom20 (Santa Cruz, sc-11415, 1:200) or CRIF1 antibody (Santacruz, sc-374122, 1:200) overnight at 4°C, incubated with the secondary antibody (anti-rabbit or anti-mouse Alexa Fluor-488, 1:1000) for 1 hour at RT. Peroxisomes were visualized using an antibody against Catalase (Abcam, ab16731, 1:200). Images were obtained analyzing z-stacks (max intensity) at multiple positions under non-saturating exposure conditions. For imaging of the dose-dependent accumulation of RNPs, HEK293T were transfected with different amounts of GFP proteins and stained with a PABPC antibody (Abcam, ab21060, 1:200) overnight at 4°C, and incubated with the secondary antibody (don key anti-rabbit Alexa 568, 1:1000) for 1 hour at RT. For all cell immunofluorescence staining, nuclei were counterstained with DAPI. To analyze granule number and area, GFP-PUM2 and PABPC co-stained samples were thresholded and double positive granules were counted for at least 20 cells from three random fields to assess the number of RNPs per cell. Co-positive PUM2 and ThS (Sigma, T1892) granules in the neocortex, hippocampus and dentate gyrus regions of mice brain tissues were counted and the granule area was calculated by using the Fiji "analyze particles" for > 20 cells. Image processing was performed with Fiji.

Worm imaging—p_{myo-3}::mito::GFP and vha-6p::GFP::daf-22 worms at the indicated ages were prepared for imaging as described in (Houtkooper et al., 2013). Briefly, worms were immobilized with tetramisole and analyzed by confocal microscopy, to assess the mitochondrial and peroxisomal morphology, and by bright-field microscopy to evaluate mitochondrial mass. The latter was analyzed by quantifying the GFP signal of single worms (n > 5) using Fiji. For Phalloidin staining, a population of 100 D8 worms was washed in M9, frozen in liquid nitrogen and lyophilized using a centrifugal evaporator. Worms were permeabilized using acetone. 2 U of phalloidin (Thermo Scientific) were resuspended in 20uL of a buffer containing: Na-phosphate pH 7,5 (final concentration 0,2mM), MgCl (final concentration 1 mM), SDS (final concentration 0,004%) and dH2O to volume, and subsequently dispensed on NGM plates. Worms were incubated on plates for 1h in the dark. Following the immobilization, worms were observed by using confocal microscopy.

Mitophagy quantitation—C2C12 transduced with the m-KEIMA were examined as described in (Zheng et al., 2017). In brief, m-KEIMA fluorescence was imaged in two channels via two sequential excitations (488 nm, cyan; 555 nm, red) and using a 570- to 695-nm emission range. Imaging settings were maintained with the same parameters for comparison between different experimental conditions. Mitophagy index quantification was performed as previously described (Zheng et al., 2017). Briefly, 550/438 signal ratio was

calculated for each region as 550/(550+438) signal, background corrected using a not m-KEIMA transfected control condition and normalized by total cell area. In each experimental condition, imaging parameters are the same for all data acquisitions.

Luciferase assay—The full-length 3′ UTR of human *MFF* mRNA was amplified by PCR with the following primers: MFF_3'UTR_Fw: 5' TTTTCTAGAAGGTAACATCAGCCCTC 3'; MFF_3'UTR_Rev: 5' TTTTCTAGATTCTTTGGTTGACAGTTTATTAAATAC 3'. The PCR product was subcloned into the pGL3-promoter vector (Promega) using the XbaI restriction enzyme (NEB, R0145) and sequenced to check the correct directionality of the inserted sequence. For the luciferase assay, Hela SCR and PUM2sh stable clones were seeded in 96 well plates and transfected with 100μg of either the pGL3-promoter (Promega) or the pGL3-Luc-MFF 3'UTR plasmid. In all conditions, the cells were co-transfected with 10μg of pRL-CMV Renilla-expressing vector. FuGENE 6 (Promega) was used as transfection reagent, following manufacturer's instructions. Cells were analyzed for both Luciferase and Renilla luminescence using the Dual-Glo® Luciferase Assay System Protocol (Promega, E2940), according to the manufacturer's instructions.

Quantitative real-time PCR (q-RT-QPCR), mtDNA/nDNA ratio and citrate synthase activity.—RNA from cells and tissues and worms was extracted using TRIzol (Thermo Scientific, 15596026) and then transcribes in cDNA by the QuantiTect Reverse Transcription Kit (Qiagen, 205313) following the manufacturer's instructions. The q-RT-PCR reactions were performed using the Light-Cycler system (Roche Applied Science) and the expression of selected genes was analysed using the LightCycler 480 System (Roche) and SYBR Green chemistry. All quantitative polymerase chain reaction (PCR) results were presented relative to the mean of housekeeping genes (ΔΔCt method). mRNA levels were normalized over *Gapdh* for gene expression for cell and tissue samples. For *C. elegans*, two housekeeping genes were used to normalize the expression data, actin (*act-1*) and peroxisomal membrane protein 3 (*pmp-3*). Relative values for mitochondrial genes (*mt-16S* for cells, *nduo-1* for worms) and nuclear genes (*Hk2* for cells, *act-3* for worms) were compared in each sample to generate a ratio representing the relative level of mtDNA per nuclear genome. The average of three technical replicates was used for each biological data point. Primer sets for quantitative reverse transcription PCR (q-RT-PCR) analyses are shown in Supplementary Table 5. Citrate synthase (CS) activity was determined using the CS assay kit (Sigma, CS0720–1KT). Absorbance at 412 nm was recorded on a Victor X4 (PerkinElmer) with 10 readings over the 1.5-min timespan. These readings were in the linear range of enzymatic activity. The difference between baseline and oxaloacetate-treated samples was obtained and used to calculate total citrate synthase activity according to the formula provided in the manual. The obtained values were normalized to the amount of protein used for each sample.

RNA-Crosslinking and Immunoprecipitation (CLIP)—C2C12 cells were plated on 150 cm culture plate and after 24 hours the medium was replaced by ice cold PBS. For CLIP from brain tissues, one brain per experimental condition was resuspended in ice-cold PBS and chunked in smaller pieces. The solution was pipetted with a glass Pasteur pipette until

dissolving all visible tissue pieces and the layered on a 10 cm culture plate. For both C2C12 cells and tissue homogenate, plates were exposed to 150 mJ/cm2 UVC (Stratagene, model UV Stratalinker 2400) on ice. Cells were then pelleted and lysed in CLIP buffer (50 mM Tris-HCl pH 7.4, 100 mM NaCl, 1% NP-40, 0.1% SDS, 0.5% sodium deoxycholate, 80 U/ml RNase OUT (Invitrogen) with protease inhibitor). Supernatants were pre-cleared with Protein A/G beads, rabbit control IgG, 0.05% BSA (Sigma, A7906–100G) and 0.2 μg/ml yeast tRNA (Thermo Scientific, AM7119). Pre-cleared lysates were incubated with PUM2 antibody (Abcam, ab10361, 5 μg) or the corresponding amount of control rabbit IgG, overnight at 4°C with gentle rotation. Next day, 40 μl of Protein A-G beads were added to the lysates and the tubes were incubated for an additional hour at 4°C with g entle rotation. Then, beads were washed 5 times with CLIP buffer. Beads were treated using 20 units of RNase-free DNase (Roche, 04716728001) for 15 min at room temperature, followed by PCR-grade Proteinase K (50 μg, Roche, RPROTKSOL-RO) treatment for 30 min at 37° C. Immunoprecipated RNA was isolated using miRNeasy kit (Qiagen, 217004) and q-RT PCR was performed using primers designed to amplify *Mff* cDNA regions flaking the PUM2-binding site. Values represent the ratio of the mRNA levels in the IP'ed fraction normalized by the levels in the corresponding total mRNA fraction. Primers are listed in Supplementary Table 5. Isolated RNA from a fraction (5%) of pre-cleared lysate was used as input.

SILAC and CoIP-LC-MS^2 proteome analysis—For SILAC labeling, HeLa SCR and *PUM2 sh* #1 clones were cultured in for six passages in SILAC DMEM media minus l-arginine and l-lysine (Thermo Scientific, 89985) with 10% dialyzed fetal bovine serum (Invitrogen) and 100 U/mL penicillin/streptomycin. Two biological replicates were performed, namely Forward (Fw) and Reverse (Rev), with the cells containing the following mixture of amino acids at 49 mg/mL each: SCR Fw, larginine (Arg0) and l-lysine (Lys0); *PUM2*sh Fw, 13C615N4-l-arginine (Arg10) and 13C615N2-l-Lysine (Lys8); SCR Rev, 13C615N4-l-arginine (Arg10) and 13C615N2-l-Lysine (Lys8), *PUM2*sh Rev, 13C614N4-l-arginine (Arg6) and 4,4,5,5-D4-l-lysine (Lys4). The SILAC-labeled cells were then lysed in SDS 2% and protein concentrations of the different lysates were estimated with DC protein assay. Samples were mixed equitably at 10μg per SILAC state per replicate. Samples were trypsin digested using the FASP protocol. Peptide were desalted on C18 StageTips and fractionated into six fractions by strong cation exchange. All fractions were dried down by vacuum centrifugation prior to Mass Spectrometric measurements. For LC MS/MS analysis, peptides were resuspended in 2% acetonitrile, 0.1% FA and separated by reversed-phase chromatography on a Dionex Ultimate 3000 RSLC nanoUPLC system in-line connected with an Orbitrap Q Exactive Mass-Spectrometer (Thermo Fischer Scientific). SILAC labeled data were analyzed with MaxQuant version 1.5.1.2 against a concatenated database consisting of UniProt human database release 2015_07. Carbamidomethylation was set as a fixed modification, whereas oxidation (M) and acetylation (Protein N-term) were considered as variable modifications. Relative quantification within different conditions was obtained calculating the significance B values for each of the identified proteins using Perseus software. Supplementary Table 1 contains the full proteomic dataset.

For the CoIP-MS/MS experiment, a whole brain per condition was lysed in CoIP buffer. 3 mg of each sample were IP'ed with PUM2 or IgG as described above. IP'ed proteins were

eluted in 5× LB and separated by SDS-PAGE. Gel was stained with Coomassie blue and gel bands were excised and In-gel digested. Briefly, the gel plugs were first washed and destained in 50% Ethanol; 50mM Ammonium Bicarbonate (AB) twice and dried by vacuum centrifugation. Samples were then reduced in 10mM Dithioerythritol (DTE) for 45min. and then alkylated in 55mM Iodoacatamide (IAA) for 30min. Over-Night digestion was performed at 37°C using Mass Spectrometry Trypsin g rade at a final concentration of 12.5 ng/µl in 50 mM AB and 10 mM CaCl2. Resulting peptides were extracted in 70% Ethanol; 5% formic acid (FA) twice and dried by vacuum centrifugation. Peptides were finally using C18 StageTips prior to LC-MS2 measurements. Chromatographic separations were performed on a Dionex Ultimate 3000 RSLC nano UPLC system (Thermo Fischer Scientific) on-line connected with a Q-Exactive HF Mass Spectrometer (Thermo Fischer Scientific). Samples were resuspended in 2% acetonitrile; 0.1% FA and captured on a capillary Pre-column (Dionex-Thermo, Acclaim PepMap 100, 75µmID × 2cm, C18 3µm 100Ä). Separations were performed on an in-site packed capillary Reverse Phase column (Reprosil Pur AQ, 75µmID × 40cm, C18 1.9µm 120Ä) at 250 nl/min. over a 90min. biphasic gradient. Mass spectrometric measurements were performed in Data Dependent mode. MS scans were acquired with a resolution of 60K using an AGC (Automatic Gain Control) of 3e6. The 7 most intense parent ions were selected and fragmented by HCD using an isolation window of 1.2m/z and a Normalised Collision Energy (NCE) of 27. Daughter ions were detected in the Orbitrap with resolutions of 45K using an AGC of 1e5. Database searches were performed in Proteome Discoverer v. 1.4 using Mascot (Matrix Science, Boston, USA) and SEQUEST as search engines against the Uniprot Mus Musculus protein database (release 2018. 07. 31). Enzyme specificity was set to Trypsin and up to two missed cleavages were allowed. Carbamidomethylation (C) was set as a fixed modification, whereas oxidation (M), acetylation (protein N-term) and phosphorylation (STY) were considered as variable modifications. A 1% FDR cut-off was fixed at peptide and protein identification levels. Scaffold v. 4.8.4 was used for the final Data display. Supplementary Table 4 contains the list of PUM2-binding proteins.

Metabolomics—HeLa stable clones were seeded at density of 3×10^5 cells/well in 6-well plates. After 48 hours, cells were washed twice with 75 mM ammonium carbonate buffer (pH 7.4, 37°C) and cell metabolism was quenched by shock freezing of plates in liquid N_2. Metabolites were extracted by adding 700 µl ice-cold acetonitrile/methanol/water (40:40:20, v/v). The extraction procedure was repeated twice. Scraped cells and supernatants were pooled in the same tube. To remove cell debris, tubes were centrifuged (4°C, 13'000 rpm, 2 min) and the supernatants collected were assayed by flow injection analysis using TOF MS (6550 QTOF, Agilent Technologies) operated in the negative ionization mode. High resolution mass spectra were recorded from 50–1,000 m/z and analyzed as described previously (Fuhrer et al., 2011). Detected ions were putatively annotated by accurate mass against the Human Metabolome Database version 3.6. Mass matching was done using a tolerance of m/z 0.001 and including isotopologues, common electrospray derivatives, and adducts. Differences between treatments and control cells were determined using the R/Bioconductor package limma. Supplementary Table 2 contains the full metabolomics dataset.

RNA sequencing library preparation and analysis—Total RNA from HeLa cells was extracted using TRIzol (Thermo Fisher Scientific) and purified by column using RNeasy Mini kit (QIAGEN, 74104). Agilent 2100 Bioanalyzer (Agilent RNA 6000 Nano Kit) was used to detect the total RNA samples concentration, RIN, 28S/18S and size. The purity of the samples was tested by NanoDrop™. Total RNA sample was digested by DNaseI (NEB) and purified by oligo-dT beads (Dynabeads mRNA purification kit, Invitrogen, 61006), then poly (A)-containing mRNA were fragmented into 130bp with First Strand buffer. First-strand cDNA was generated by N6 primer, FirstStrand Master Mix and Super Script II reverse transcription (Invitrogen, 18064022) (Reaction condition: 25°C for 10 min; 42°C or 40 min; 70°C for 15 min). Then Second Strand Master Mix was added to synthesize the second-strand cDNA (16°C for 1h). The cDNA was purified with Ampure XP Beads (Agencourt, A63880), combined with End Repair Mix, incubated at 20°C for 30min, purified, added with A -Tailing Mix and incubated at 37°C for 30 min. Then the samples were combined with Adenylate 3' Ends DNA, Adapter and Ligation Mix and incubated for the ligation reaction at 20°C for 20 min. Several rounds of PCR amplification with PCR Primer Cocktail and PCR Master Mix were performed to enrich the cDNA fragments. Then the PCR products were purified with Ampure XP Beads. The final library was quantitated in two ways: determining the average molecule length using the Agilent 2100 bioanalyzer (Agilent DNA 1000 Reagents), and quantifying the library by real-time quantitative PCR (QPCR) (TaqMan Probe). The libraries were amplified on cBot to generate the cluster on the flow cell (TruSeq PE Cluster Kit V3–cBot–HS, Illumina, PE-401–3001) and the amplified flow cell was sequenced pair end on the HiSeq 2000 System (TruSeq SBS KIT-HS V3, Illumina, TG-101–3001), with read length 50bp. The reads obtained were first trimmed out to remove adaptor sequences and then mapped using a TopHat2 against the human genome (GRCh37). HTSeq-count was then used to obtain the counts of each gene. Differential expressed genes in each condition were identified using R/Bioconductor package Deseq. Supplementary Table 3 contains the full RNA-seq dataset.

Mitochondria respiration assessment—Oxygen consumption rate (OCR) was assessed in gastrocnemius mechanically homogenized in mitochondrial respiration medium (mir05: EGTA 0.5mM, MgCl2.6H2O 3mM, Taurine 20mM, KH2PO4 10mM, HEPES 20mM, D-Sucrose 110mM, BSA essentially fatty-acid free 1g/l, Lactobionic Acid 60mM, pH 7.1) by high resolution respirometry (Oxygraph 2k, Oroboros Instruments) following manufactures' instructions. Pyruvate (5mM), Malate (2mM), Glutamate (10mM), Succinate (10mM) and ADP+Mg2+ (1.25mM) were added directly into the 2ml-chamber to assess State3ADP respiration driven by complexes I and II. CI-inhibitor Rotenone (0.1 μM) was used to assess CII-driven respiration and CIII-inhibitor Antimycin A (2.5 μM) was used to control for nonmitochondrial respiration.

RNPs fractionation assay—Cytosolic and RNP fractions were isolated from whole brain extracts of young and old mice adapting the protocol described in (Wheeler et al., 2017). Briefly, snap frozen brains were powdered, resuspended in Stress granule lysis buffer and homogenized (30 strokes, 1500 rpm). Samples were centrifuged as in (Wheeler et al., 2017). Equal amounts of RNP and cytosolic extracts were analysed by western blot and their purity was assessed using STAU1 and GAPDH, respectively.

CRISPR-Cas9 plasmid cloning—Guide RNAs targeting the *Pum2* gene were designed using the CRISPR Benchling design software (https://benchling.com/crispr, gRNA length = 21bp with additional 5′ guanine, PAM = NNGRRT), selecting the first 3 hits, ranked by the On-target score. The primers were designed and cloned in the HA-saCas9/containing px601 plasmid, as described in (Ran et al., 2015), to obtain the following plasmids: g*PUM2* #1, #2 and #3. The primers used for the cloning are listed in the Supplementary Table 5. For the guide efficiency determination, 3mg of g*PUM2*sh#1, #2, #3 and px601 as control were transfected in HEK293T with Fugene6, following manufacturer's instructions. After 48 hours, cells were lysed in RIPA buffer and analyzed by Western Blot as described above. g*PUM2* #1 was selected as the most efficient guide and its genome editing efficiency was further confirmed by sequencing the genomic region containing the g*PUM2* #1-targeted sequence. Genomic DNA from cells transfected with the g*PUM2*#1 and the px601 plasmids was extracted with the NucleoSpin® Tissue kit (Macherey-Nagel, 740952). The PCR was performed using the oligos listed in the Supplementary Table 5. The PCR product was gel purified and Sanger sequenced with the PCR Fw oligo. PCR products were analyzed for % of indels and of aberrant sequences using TIDE (https://www.deskgen.com/landing/tide.html). ΔPBE-*Mff* UP and DOWN oligo, listed in in the Supplementary Table 5, were designed to encompass the PBE of *Mff* 3'UTR and were cloned in the LentiCRISPR v.2 plasmid (Addgene # 52961) to obtain PBE-*Mff*-UP and PBE-*Mff*-Down plasmids. C2C12 were transfected with both plasmids, selected with puromycin 24 hours after transfection and single cells sorted after additional 48 hours. Clones were then grown without selection marker. Cellular gDNA was extracted and a PCR was performed using the oligo listed in the Supplementary Table 5. The PCR product was gel purified and Sanger sequenced with the PCR Fw oligo and one clone lacking *Mff's* PBE was renamed ΔPBE-*Mff* and used for further experiments.

Adeno associated virus (AAV) production—Recombinant serotype 9 adeno-associated viral (AAV) vectors were produced according to standard procedures, as described in (Löw et al., 2013). Briefly, HEK AAV-293 cells (Agilent) were co-transfected with the pAAV (px601 or px601-g*PUM2*sh#1) and pDP9 plasmids. The AAV9 particles contained in the cell lysates were isolated on an iodixanol gradient followed by ion exchange FPLC using a HiTrap Q-FF column (5 ml, GE Healthcare) connected to an AKTA start chromatography system (GE Healthcare). After buffer exchange (resuspension in DPBS) and concentration on a centrifugal filter (cut-off 100 kDa, Amicon Ultra, Millipore), the vector suspensions were titered by real-time PCR for the presence of genome-containing particles (VG), as described in (D'Costa et al., 2016). The titers of the obtained AAV9 suspensions used for in vivo experiments ranged between 7.9E13 VG/mL and 2.4E14 VG/mL.

Transmission electron microscopy—24 months old male C57BL/6J mice were perfused, via the heart, with 200 ml of a buffered mix of 2.5 % glutaraldehyde and 2.0 % paraformaldehyde in 0.1M phosphate buffer (pH 7.4), and then left for 30 minutes. The gastrocnemius muscle was then removed and the medial portion sliced into small (1 × 1 × 1 mm) cubes which were then further fixed in the same fixative solution for a further 4 hours. The cubes were then washed thoroughly with cacodylate buffer (0.1M, pH 7.4), postfixed

for 40 minutes in 1.0 % osmium tetroxide with 1.5% potassium ferrocyanide, and then in 1.0% osmium tetroxide for a further 40 minutes alone. They were finally stained for 30 minutes in 1% uranyl acetate in water before being dehydrated through increasing concentrations of alcohol and then embedded in Durcupan ACM (Fluka, Switzerland) resin. The samples were then placed in silicon molds and left to harden for 24 hours in a 65°C oven. Thin, 50 nm thi ck, sections were cut with a diamond knife, and collected onto pioloform support films on single slot copper grids. These were contrasted with lead citrate and uranyl acetate, and images taken with a transmission electron microscope at 80 kV (Tecnai Spirit, FEI Company with Eagle CCD camera). To analyse the morphology of mitochondria we used block face scanning electron microscopy. The fixed muscle tissue was cut into small cubes (1 mm × 1 mm) and immersed in a buffered mix of paraformaldehyde (1%) and glutaraldehyde (1.25%). After 24 hours, the pieces were postfixed in potassium ferrocyanide (1.5%) and osmium (2%), then stained with thiocarbohydrazide (1%) followed by osmium tetroxide (2%) and then stained overnight in uranyl acetate (1%). Sections where washed in water at 50°C before being stained with lead aspartate at the same temperature. The sections were then dehydrated in increasing concentrations of ethanol and then embedded in spurs resin which was hardened at 65 degrees for 24 h. Samples were glued to aluminum mounting pins and mounted inside the electron microscope (Zeiss Merlin) fitted with a 3View system (Gatan). Serial images were collected of the region of interest at 1.5 kV using a pixel size of around 6 nm and 50 nm of resin was removed from the block surface after each image. The final image series was aligned within the TrakEM2 plugin (Fiji) and then segmented using the arealist function. The final models were then imported into the Blender software (www.blender.org) and the volumes of mitochondria measured using the NeuroMorph toolset (Jorstad et al., 2015) (www.neuromorph.epfl.ch).

Bioinformatic and statistical analysis—For the *in silico* correlation of *Pum2* expression levels with longevity, we used publicly available longevity data from the BXD (mean longevity) and LXS genetic reference population (maximal longevity) downloaded from GeneNetwork.org. Pearson's *r* was used to establish correlations between longevity and *Pum2* mRNA levels in whole brain and neocortex respectively. For the GSEA, RNAseq data from human tissues, as well as the covariates data, were downloaded from the GTEx Portal (version v6p) (GTEx Consortium, 2013). Gene expression residuals after removing the available covariates by PEER were used for the enrichment analysis. For enrichment analysis, genes were ranked based on their Pearson correlation coefficients with the expression residuals of *PUM2*, and Gene Set Enrichment Analysis (GSEA) was performed to find the enriched gene sets co-expressed with *PUM2* (Subramanian et al., 2005) by using R/fgsea package. The corrgram was obtained using the R/corrgram package, using the Muscle mRNA expression levels of the indicated human genes, downloaded from GeneNetwork.org/GTEx v.5. The depth of the shading at the correlation matrices indicates the magnitude of the correlation (Pearson's r). Positive and negative correlations within the corrgram are represented in blue and red, respectively. Heatmaps were obtained using the heatmap2 function of R/gplots. The network analysis was performed using Cytoscape 7.0 with the STRING interaction database. Pathway enrichment analysis for Gene Ontology (GO) Cellular Component and Molecular Function and for Reactome was performed using EnrichR (http://amp.pharm.mssm.edu/Enrichr/).

Quantification and Statistical Analysis

No statistical methods were used to predetermine sample size. Differences between two groups were assessed using two-tailed t-tests, unless stated otherwise. Differences between more than two groups were assessed by using one-way ANOVA. For worm lifespan analysis, log-rank (Mantel-Cox) test was used to compare two different groups. GraphPad Prism 6 (GraphPad Software, Inc.) was used for all statistical analyses. Variability in plots and graphs is presented as the standard deviation (s.d.), unless stated otherwise. All $p< 0.05$ were considered to be significant. *$p < 0.05$; **$p \leq 0.01$; ***$p \leq 0.001$; ****$p \leq 0.0001$ unless stated otherwise. Mouse experiments were performed once. Animals that showed signs of severity, predefined by the animal authorizations, were euthanized. These animals, together with those who died spontaneously during the experiments, were excluded from the calculations. These criteria were established before starting the experiments. For motility, fitness and death scoring experiments in *C. elegans*, sample size was estimated based on the known variability of the assay. All experiments were done non-blinded and repeated at least twice.

Supplementary Material

Refer to Web version on PubMed Central for supplementary material.

Acknowledgments

We are grateful to P. Gönczy and M. Pierron (EPFL) for sharing reagents, the Caenorhabditis Genetics Center, for providing worm strains. The EPFL-Proteomics facility. Jessica Dessimoz and Gian-Filippo Mancini, Catherine Maclachlan for help with experiments. Michael Kiebler kindly sharied the GFP-PUM2 plasmid. D.D. was supported by a fellowship of the Associazione Italiana per la Ricerca sul Cancro (AIRC) and Marie Curie Actions. V.S. is supported by the 'EPFL Fellows' program co-funded by the Marie Skłodowska-Curie, Horizon 2020 Grant agreement (665667). This research project in the J,A. lab was supported by the EPFL, NIH (R01AG043930), Systems X (SySX.ch 2013/153), Velux Stiftung (1019), the FSRMM, the SNF (310030B_160318) and the Fondation Levaillant.

Declaration of Interests

EPFL filed a patent application on the work represented in this study and DDA and JA are listed as inventors.

References

Anders S, Pyl PT, and Huber W (2015). HTSeq—a Python framework to work with high-throughput sequencing data. Bioinformatics 31, 166–169. [PubMed: 25260700]

Apicco DJ, Ash PEA, Maziuk B, LeBlang C, Medalla M, Abdullatif AA, Ferragud A, Botelho E, Ballance HI, Dhawan U, et al. (2018). Reducing the RNA binding protein TIA1 protects against tau-mediated neurodegeneration in vivo. Nat. Neurosci 21, 72. [PubMed: 29273772]

Arantes-Oliveira N, Apfeld J, Dillin A, and Kenyon C (2002). Regulation of life-span by germ-line stem cells in Caenorhabditis elegans. Science 295, 502–505. [PubMed: 11799246]

Banerjee A, Apponi LH, Pavlath GK, and Corbett AH (2013). PABPN1: molecular function and muscle disease. FEBS J. 280, 4230–4250. [PubMed: 23601051]

Bohn JA, Van Etten JL, Schagat TL, Bowman BM, McEachin RC, Freddolino PL, and Goldstrohm AC (2017). Identification of diverse target RNAs that are functionally regulated by human Pumilio proteins. Nucleic Acids Res.

Burman JL, Pickles S, Wang C, Sekine S, Vargas JNS, Zhang Z, Youle AM, Nezich CL, Wu X, Hammer JA, et al. (2017). Mitochondrial fission facilitates the selective mitophagy of protein aggregates. J Cell Biol jcb.201612106.

Chaturvedi P, Neelamraju Y, Arif W, Kalsotra A, and Janga SC (2015). Uncovering RNA binding proteins associated with age and gender during liver maturation. Sci. Rep 5, 9512. [PubMed: 25824884]

Chen H, Ren S, Clish C, Jain M, Mootha V, McCaffery JM, and Chan DC (2015). Titration of mitochondrial fusion rescues Mff-deficient cardiomyopathy. J. Cell Biol 211, 795–805. [PubMed: 26598616]

D'Costa S, Blouin V, Broucque F, Penaud-Budloo M, François A, Perez IC, Le Bec C, Moullier P, Snyder RO, and Ayuso E (2016). Practical utilization of recombinant AAV vector reference standards: focus on vector genomes titration by free ITR qPCR. Mol. Ther. Methods Clin. Dev 5, 16019. [PubMed: 27069952]

Edwards MG, Anderson RM, Yuan M, Kendziorski CM, Weindruch R, and Prolla TA (2007). Gene expression profiling of aging reveals activation of a p53-mediated transcriptional program. BMC Genomics 8, 80. [PubMed: 17381838]

Etten JV, Schagat TL, Hrit J, Weidmann CA, Brumbaugh J, Coon JJ, and Goldstrohm AC (2012). Human Pumilio Proteins Recruit Multiple Deadenylases to Efficiently Repress Messenger RNAs. J. Biol. Chem 287, 36370–36383. [PubMed: 22955276]

Fox M, Urano J, and Reijo Pera RA (2005). Identification and characterization of RNA sequences to which human PUMILIO-2 (PUM2) and deleted in Azoospermia-like (DAZL) bind. Genomics 85, 92–105. [PubMed: 15607425]

Frank M, Duvezin-Caubet S, Koob S, Occhipinti A, Jagasia R, Petcherski A, Ruonala MO, Priault M, Salin B, and Reichert AS (2012). Mitophagy is triggered by mild oxidative stress in a mitochondrial fission dependent manner. Biochim. Biophys. Acta 1823, 2297–2310. [PubMed: 22917578]

Gandre-Babbe S, and van der Bliek AM (2008). The Novel Tail-anchored Membrane Protein Mff Controls Mitochondrial and Peroxisomal Fission in Mammalian Cells. Mol. Biol. Cell 19, 2402–2412. [PubMed: 18353969]

Gelman R, Watson A, Bronson R, and Yunis E (1988). Murine Chromosomal Regions Correlated with Longevity. Genetics 118, 693–704. [PubMed: 3163317]

Gitler AD, and Shorter J (2011). RNA-binding proteins with prion-like domains in ALS and FTLD-U. Prion 5, 179–187. [PubMed: 21847013]

Gonskikh Y, and Polacek N (2017). Alterations of the translation apparatus during aging and stress response. Mech. Ageing Dev. 168, 30–36. [PubMed: 28414025]

Consortium GTEx (2013). The Genotype-Tissue Expression (GTEx) project. Nat. Genet 45, 580–585. [PubMed: 23715323]

Hafner M, Landthaler M, Burger L, Khorshid M, Hausser J, Berninger P, Rothballer A, Ascano M, Jungkamp A-C, Munschauer M, et al. (2010). Transcriptome-wide identification of RNA-binding protein and microRNA target sites by PAR-CLIP. Cell 141, 129–141. [PubMed: 20371350]

Harrison AF, and Shorter J (2017). RNA-binding proteins with prion-like domains in health and disease. Biochem. J 474, 1417–1438. [PubMed: 28389532]

Houtkooper RH, Williams RW, and Auwerx J (2010). Metabolic Networks of Longevity. Cell 142, 9–14. [PubMed: 20603007]

Houtkooper RH, Mouchiroud L, Ryu D, Moullan N, Katsyuba E, Knott G, Williams RW, and Auwerx J (2013). Mitonuclear protein imbalance as a conserved longevity mechanism. Nature 497, 451–457. [PubMed: 23698443]

Huang EJ, Zhang J, Geser F, Trojanowski JQ, Strober JB, Dickson DW, Brown RH, Shapiro BE, and Lomen-Hoerth C (2010). Extensive FUS-immunoreactive Pathology in Juvenile Amyotrophic Lateral Sclerosis with Basophilic Inclusions. Brain Pathol. Zurich Switz. 20, 1069–1076.

Jorstad A, Nigro B, Cali C, Wawrzyniak M, Fua P, and Knott G (2015). NeuroMorph: A Toolset for the Morphometric Analysis and Visualization of 3D Models Derived from Electron Microscopy Image Stacks. Neuroinformatics 13, 83–92. [PubMed: 25240318]

Kageyama Y, Hoshijima M, Seo K, Bedja D, Sysa-Shah P, Andrabi SA, Chen W, Höke A, Dawson VL, Dawson TM, et al. (2014). Parkin-independent mitophagy requires Drp1 and maintains the integrity of mammalian heart and brain. EMBO J. 33, 2798–2813. [PubMed: 25349190]

Kamath RS, Martinez-Campos M, Zipperlen P, Fraser AG, and Ahringer J (2001). Effectiveness of specific RNA-mediated interference through ingested double-stranded RNA in Caenorhabditis elegans. Genome Biol. 2, RESEARCH0002. [PubMed: 11178279]

Katayama H, Kogure T, Mizushima N, Yoshimori T, and Miyawaki A (2011). A Sensitive and Quantitative Technique for Detecting Autophagic Events Based on Lysosomal Delivery. Chem. Biol 18, 1042–1052. [PubMed: 21867919]

Koopman M, Michels H, Dancy BM, Kamble R, Mouchiroud L, Auwerx J, Nollen EAA, and Houtkooper RH (2016). A screening-based platform for the assessment of cellular respiration in Caenorhabditis elegans. Nat. Protoc 11, 1798–1816. [PubMed: 27583642]

Lechler MC, Crawford ED, Groh N, Widmaier K, Jung R, Kirstein J, Trinidad JC, Burlingame AL, and David DC (2017). Reduced Insulin/IGF-1 Signaling Restores the Dynamic Properties of Key Stress Granule Proteins during Aging. Cell Rep 18, 454–467. [PubMed: 28076789]

Leduc-Gaudet J-P, Picard M, Pelletier FS-J, Sgarioto N, Auger M-J, Vallée J, Robitaille R, St-Pierre DH, Gouspillou G, Leduc-Gaudet J-P, et al. (2015). Mitochondrial morphology is altered in atrophied skeletal muscle of aged mice. Oncotarget 6, 17923–17937. [PubMed: 26053100]

Lee S, Kopp F, Chang T-C, Sataluri A, Chen B, Sivakumar S, Yu H, Xie Y, and Mendell JT (2016). Noncoding RNA NORAD Regulates Genomic Stability by Sequestering PUMILIO Proteins. Cell 164, 69–80. [PubMed: 26724866]

Lee Y, Jonson PH, Sarparanta J, Palmio J, Sarkar M, Vihola A, Evilä A, Suominen T, Penttilä S, Savarese M, et al. (2018). *TIA1* variant drives myodegeneration in multisystem proteinopathy with *SQSTM1* mutations. J. Clin. Invest 128.

Liao C-Y, Rikke BA, Johnson TE, Diaz V, and Nelson JF (2010). Genetic Variation in the Murine Lifespan Response to Dietary Restriction: from Life Extension to Life Shortening. Aging Cell 9, 92–95. [PubMed: 19878144]

Löw K, Aebischer P, and Schneider BL (2013). Direct and retrograde transduction of nigral neurons with AAV6, 8, and 9 and intraneuronal persistence of viral particles. Hum. Gene Ther. 24, 613–629. [PubMed: 23600720]

Masuda K, Marasa B, Martindale JL, Halushka MK, and Gorospe M (2009). Tissue- and age-dependent expression of RNA-binding proteins that influence mRNA turnover and translation. Aging 1, 681–698. [PubMed: 20157551]

Maziuk BF, Apicco DJ, Cruz AL, Jiang L, Ash PEA, da Rocha EL, Zhang C, Yu WH, Leszyk J, Abisambra JF, et al. (2018). RNA binding proteins co-localize with small tau inclusions in tauopathy. Acta Neuropathol. Commun 6, 71. [PubMed: 30068389]

Molliex A, Temirov J, Lee J, Coughlin M, Kanagaraj AP, Kim HJ, Mittag T, and Taylor JP (2015). Phase separation by low complexity domains promotes stress granule assembly and drives pathological fibrillization. Cell 163, 123–133. [PubMed: 26406374]

Mouchiroud L, Houtkooper RH, Moullan N, Katsyuba E, Ryu D, Cantó C, Mottis A, Jo Y-S, Viswanathan M, Schoonjans K, et al. (2013). The NAD+/Sirtuin Pathway Modulates Longevity through Activation of Mitochondrial UPR and FOXO Signaling. Cell 154, 430–441. [PubMed: 23870130]

Mouchiroud L, Sorrentino V, Williams EG, Cornaglia M, Frochaux MV, Lin T, Nicolet-Dit-Félix AA, Krishnamani G, Ouhmad T, Gijs MAM, et al. (2016). The Movement Tracker: A Flexible System for Automated Movement Analysis in Invertebrate Model Organisms. Curr. Protoc. Neurosci 77, 8.37.1–8.37.21. [PubMed: 27696358]

Neelamraju Y, Hashemikhabir S, and Janga SC (2015). The human RBPome: from genes and proteins to human disease. J. Proteomics 127, 61–70. [PubMed: 25982388]

Oberdoerffer P, Michan S, McVay M, Mostoslavsky R, Vann J, Park S-K, Hartlerode A, Stegmuller J, Hafner A, Loerch P, et al. (2008). SIRT1 redistribution on chromatin promotes genomic stability but alters gene expression during aging. Cell 135, 907–918. [PubMed: 19041753]

Otera H, Wang C, Cleland MM, Setoguchi K, Yokota S, Youle RJ, and Mihara K (2010). Mff is an essential factor for mitochondrial recruitment of Drp1 during mitochondrial fission in mammalian cells. J. Cell Biol 191, 1141–1158. [PubMed: 21149567]

Palikaras K, Lionaki E, and Tavernarakis N (2015). Balancing mitochondrial biogenesis and mitophagy to maintain energy metabolism homeostasis. Cell Death Differ. 22, 1399–1401. [PubMed: 26256515]

Palikaras K, Lionaki E, and Tavernarakis N (2018). Mechanisms of mitophagy in cellular homeostasis, physiology and pathology. Nat. Cell Biol 20, 1013–1022. [PubMed: 30154567]

Ran FA, Cong L, Yan WX, Scott DA, Gootenberg JS, Kriz AJ, Zetsche B, Shalem O, Wu X, Makarova KS, et al. (2015). In vivo genome editing using Staphylococcus aureus Cas9. Nature 520, 186–191. [PubMed: 25830891]

Rana A, Oliveira MP, Khamoui AV, Aparicio R, Rera M, Rossiter HB, and Walker DW (2017). Promoting Drp1-mediated mitochondrial fission in midlife prolongs healthy lifespan of Drosophila melanogaster. Nat. Commun 8, 448. [PubMed: 28878259]

Ryu D, Mouchiroud L, Andreux PA, Katsyuba E, Moullan N, Nicolet-dit-Félix AA, Williams EG, Jha P, Lo Sasso G, Huzard D, et al. (2016). Urolithin A induces mitophagy and prolongs lifespan in C. elegans and increases muscle function in rodents. Nat. Med 22, 879–888. [PubMed: 27400265]

Schlissel G, Krzyzanowski MK, Caudron F, Barral Y, and Rine J (2017). Aggregation of the Whi3 protein, not loss of heterochromatin, causes sterility in old yeast cells. Science 355, 1184–1187. [PubMed: 28302853]

Sergushichev A (2016). An algorithm for fast preranked gene set enrichment analysis using cumulative statistic calculation. BioRxiv 060012.

Sheinberger J, and Shav-Tal Y (2017). mRNPs meet stress granules. FEBS Lett. 591, 2534–2542. [PubMed: 28746974]

Shi Z, and Barna M (2015). Translating the genome in time and space: specialized ribosomes, RNA regulons, and RNA-binding proteins. Annu. Rev. Cell Dev. Biol 31, 31–54. [PubMed: 26443190]

Spassov D, and Jurecic R (2003). The PUF Family of RNA-binding Proteins: Does Evolutionarily Conserved Structure Equal Conserved Function? IUBMB Life 55, 359–366. [PubMed: 14584586]

Steffen KK, and Dillin A (2016). A Ribosomal Perspective on Proteostasis and Aging. Cell Metab. 23, 1004–1012. [PubMed: 27304502]

Su J, Ekman C, Oskolkov N, Lahti L, Ström K, Brazma A, Groop L, Rung J, and Hansson O (2015). A novel atlas of gene expression in human skeletal muscle reveals molecular changes associated with aging. Skelet. Muscle 5, 35. [PubMed: 26457177]

Subramaniam K, and Seydoux G (2003). Dedifferentiation of primary spermatocytes into germ cell tumors in C. elegans lacking the pumilio-like protein PUF-8. Curr. Biol. CB 13, 134–139. [PubMed: 12546787]

Subramanian A, Tamayo P, Mootha VK, Mukherjee S, Ebert BL, Gillette MA, Paulovich A, Pomeroy SL, Golub TR, Lander ES, et al. (2005). Gene set enrichment analysis: a knowledge-based approach for interpreting genome-wide expression profiles. Proc. Natl. Acad. Sci. U. S. A 102, 15545–15550. [PubMed: 16199517]

Sun N, Youle RJ, and Finkel T (2016). The Mitochondrial Basis of Aging. Mol. Cell 61, 654–666. [PubMed: 26942670]

Tanaka A, Cleland MM, Xu S, Narendra DP, Suen D-F, Karbowski M, and Youle RJ (2010). Proteasome and p97 mediate mitophagy and degradation of mitofusins induced by Parkin. J. Cell Biol 191, 1367–1380. [PubMed: 21173115]

Twig G, Elorza A, Molina AJA, Mohamed H, Wikstrom JD, Walzer G, Stiles L, Haigh SE, Katz S, Las G, et al. (2008). Fission and selective fusion govern mitochondrial segregation and elimination by autophagy. EMBO J. 27, 433–446. [PubMed: 18200046]

Vessey JP, Schoderboeck L, Gingl E, Luzi E, Riefler J, Di Leva F, Karra D, Thomas S, Kiebler MA, and Macchi P (2010). Mammalian Pumilio 2 regulates dendrite morphogenesis and synaptic function. Proc. Natl. Acad. Sci. U. S. A 107, 3222–3227. [PubMed: 20133610]

Wheeler JR, Jain S, Khong A, and Parker R (2017). Isolation of yeast and mammalian stress granule cores. Methods San Diego Calif 126, 12–17.

Yamashita S-I, Jin X, Furukawa K, Hamasaki M, Nezu A, Otera H, Saigusa T, Yoshimori T, Sakai Y, Mihara K, et al. (2016). Mitochondrial division occurs concurrently with autophagosome formation but independently of Drp1 during mitophagy. J. Cell Biol. 215, 649–665. [PubMed: 27903607]

Yang J, Huang T, Petralia F, Long Q, Zhang B, Argmann C, Zhao Y, Mobbs CV, Schadt EE, Zhu J, et al. (2015). Synchronized age-related gene expression changes across multiple tissues in human and the link to complex diseases. Sci. Rep 5, 15145. [PubMed: 26477495]

Yasuda K, Ishii T, Suda H, Akatsuka A, Hartman PS, Goto S, Miyazawa M, and Ishii N (2006). Age-related changes of mitochondrial structure and function in Caenorhabditis elegans. Mech. Ageing Dev 127, 763–770. [PubMed: 16893561]

Zheng L, Bernard-Marissal N, Moullan N, D'Amico D, Auwerx J, Moore DJ, Knott G, Aebischer P, and Schneider BL (2017). Parkin functionally interacts with PGC-1α to preserve mitochondria and protect dopaminergic neurons. Hum. Mol. Genet 26, 582–598. [PubMed: 28053050]

Highlights

- PUM2, and its orthologue in *C. elegans*, PUF-8, are upregulated upon aging.
- PUM2 represses *Mff* translation and impairs mitochondrial fission.
- The PUM2/MFF axis regulates mitophagy and mitochondrial function.
- Depletion of *puf-8* and *Pum2* in old worms and mice improves mitochondrial homeostasis.

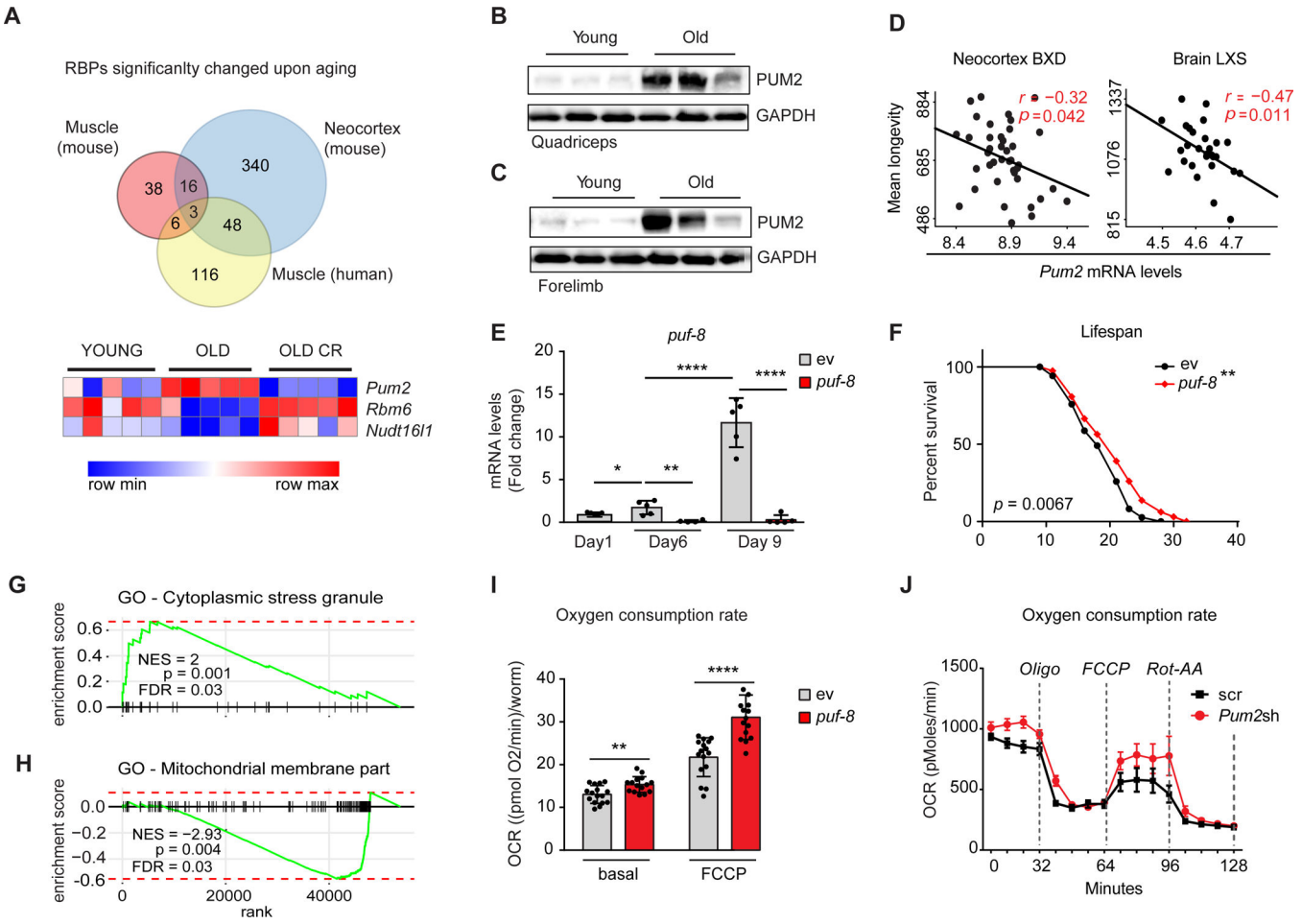

Figure 1. Pumilio2 expression is up-regulated upon aging.

(A) Top, Venn diagram representing common significantly changed transcripts amongst 1343 different RBPs in old *vs.* young and old caloric restricted *vs.* old mouse gastrocnemius muscle (from GSE6323, p < 0.05), young *vs.* old mouse neocortex tissues (from GSE13120, p< 0.001) and muscle biopsies from aged humans (Yang et al., 2015). The expression of the 3 common hits, *Pum2*, *Rbm6* and *Nudt16l1*, in GSE6323 is shown in the heatmap below.

(B and C) Western blot of PUM2 and GAPDH as loading control in young (2 month) and old (24 month) quadriceps (B) and forelimb (C) muscles from C57BL/6J mice.

(D) Correlation analysis of *Pum2* mRNA levels in neocortex from the BXD (left) and whole brain tissues from the LXS (right) mouse genetic reference populations, respectively, and mean longevity. Coefficient of correlation (*r*) and p value (*p*) in red. (E) *puf-8* mRNA levels in *glp-1(e2144)* young (Day 1), adult (Day 6) and old (Day 9) worms fed, from Day 1, with either control (ev) or *puf-8* RNAi (n = 5). *p < 0.05; **p < 0.01; ****p < 0.0001, unpaired two-tailed Student's t test. Error bars represent mean ± SD

(F) Lifespan curves of *glp-1* worms fed with empty vector (ev) or *puf-8* RNAi (*puf-8*), from Day 1 of adulthood. **p < 0.05, log-rank (Mantel-Cox) test.

(G and H) GSEA of *PUM2* in human cortex indicates its positive correlation with the gene ontology (GO) category "Cytoplasmic stress granule" (G) and negative correlation with the

category "Mitochondrial membrane part" (H). NES, normalized enrichment score. FDR, false discovery rate.

(I) Oxygen consumption rates (OCR) showing basal and FCCP-induced maximal respiration in *glp-1* worms fed as in Figure 1E. **p < 0.01; ****p < 0.0001, unpaired two-tailed Student's t test. Error bars represent the mean ± SD.

(J) OCR in C2C12 myoblasts expressing a control (SCR) or a *Pum2*-targeting shRNA treated with oligomycin (Oligo), FCCP and rotenone/antimycin A (Rot-AA). Error bars represent the mean ± SEM.

See also Figures S1 and S2.

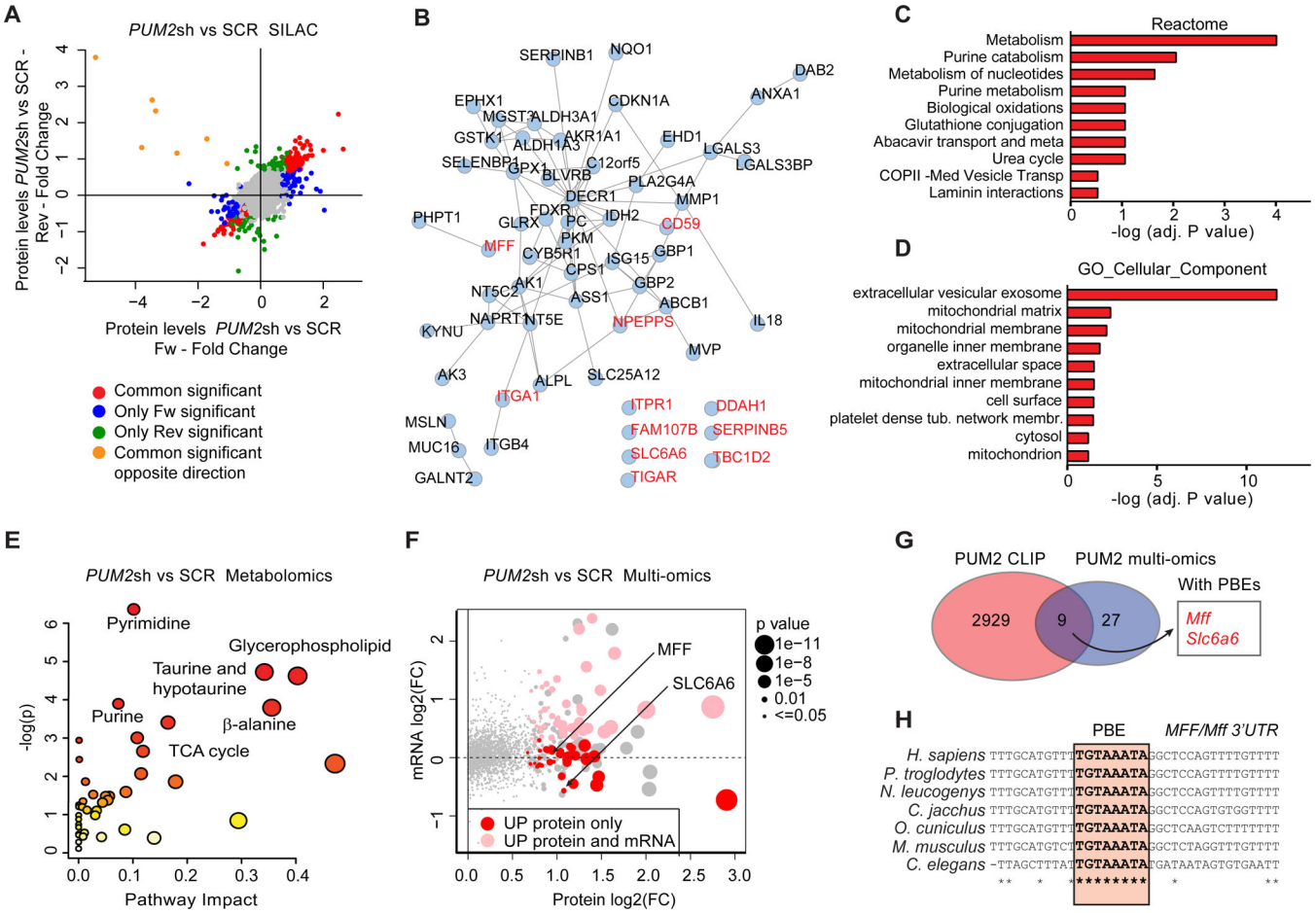

Figure 2. Multi-omics analyses reveal PUM2 as negative regulator of mitochondrial function.

(A) Proteomic changes in HeLa cells stably expressing either a scramble (SCR) or a *PUM2*-targeting short-hairpin sequence (*PUM2*sh). Scatterplot depicts SILAC Forward (Fw, x-axis) and Reverse (Rev, y-axis) replicates comparing *PUM2*sh *vs.* SCR cells. Each dot represents a single protein level, expressed as fold-change. In red are the proteins significantly regulated in both replicates (sign.B < 0.05) and with common direction of their fold change. Supplementary Table 1 contains the full proteomics dataset.

(B) STRING Interaction network of the commonly upregulated proteins from Figure 2A (interaction score > 0.500). Proteins containing at least one PBE are in red. Proteins not connected to the network are not shown, except if they contain PBEs.

(C and D) Pathway enrichment analysis for the Reactome (C) and GO Cellular component categories (D) of the 85 commonly induced proteins upon *PUM2*sh in HeLa stable clones.

(E) Metabolome pathway enrichment analysis of up-regulated metabolites in *PUM2*sh vs SCR HeLa cells. Scatter-plot represents p values from integrated enrichment analysis and impact values from pathway topology analysis. The node color is based on the p values and the node radius represents the pathway impact values. Supplementary Table 2 contains the list of all metabolites.

(F) Scatterplot of the log2(Fold change) of proteins (Fw-SILAC) and mRNAs (RNA-seq) comparing *PUM2*sh vs SCR HeLa cells. Dot size indicates the Fw-SILAC sign.B. Light-red

dots highlight hits that are upregulated at both protein and mRNA level (Fw/Rev-SILAC, sign.B < 0.05; RNA-seq, adj.p.val < 0.05). Red dots indicate hits induced at protein levels and but whose mRNA levels are not changed or downregulated (adj.p.val < 0.05). Arrows correspond to MFF and SLC6A6. Supplementary Table 3 contains the RNA-seq dataset.
(G) Venn diagram representing mRNAs bound by PUM2 (PUM2 CLIP, from (Hafner et al., 2010)) and proteins in red from Figure 2F. MFF and SLC6A6 are the only proteins whose corresponding mRNAs contain at least one PBE.
(H) Alignment of the *MFF*/*Mff* 3'UTR regions containing the PBE in the indicated species. The square highlights the evolutionary conservation of the PBE sequence. Asterisks indicate positions with fully conserved residues.
See also Figure S3 and Tables S1, S2 and S3.

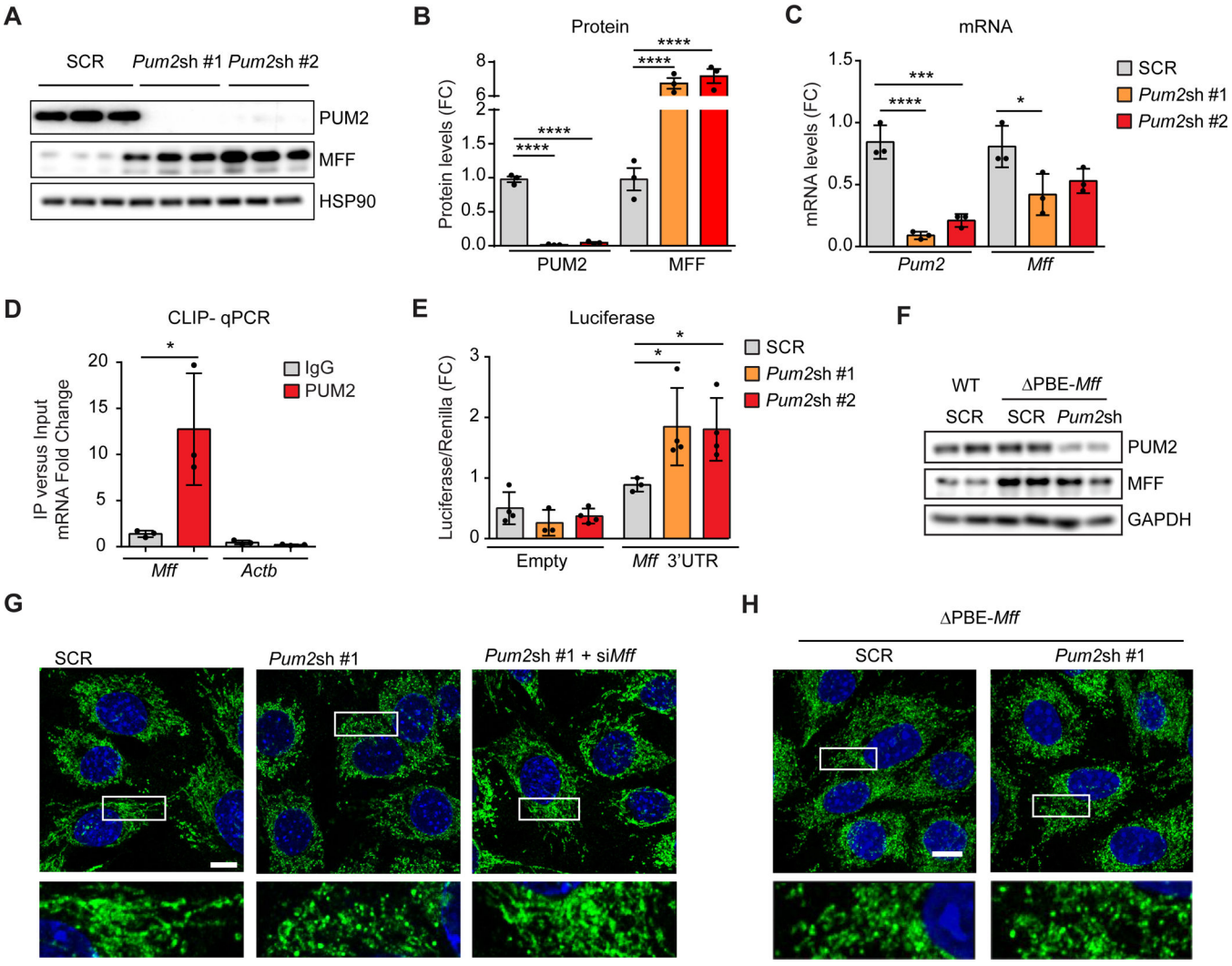

Figure 3. PUM2 regulates mitochondrial fission via MFF.

(A) Western blot of PUM2, MFF and HSP90 (as loading control) in mouse myoblast C2C12 stable cell clones, expressing a control shRNA (SCR) or two independent *Pum2*-targeting shRNAs (*Pum2*sh #1 and #2) (n=3).

(B) Quantification of PUM2 and MFF protein levels, relative to HSP90, from Figure 3A. ****p < 0.0001, one-way ANOVA. Error bars represent the mean ± SD.

(C) Quantitative-RT-PCR (q-RT-PCR) of *Pum2* and *Mff* normalized to *Gapdh* mRNA levels in C2C12 clones as in Figure 3A. Data are expressed as fold change (n = 3). *p < 0.05; ***p < 0.001, ****p < 0.0001, one-way ANOVA. Error bars represent the mean ± SD.

(D) CLIP using PUM2 or IgG (as control) in C2C12 cells(n = 3). *p < 0.05, unpaired two-tailed Student's t test. Error bars represent the mean ± SD.

(E) Luciferase assay in C2C12 SCR, *Pum2*sh #1 and *Pum2*sh #2 clones expressing the pGL3-Promoter vector containing either the *Mff* 3'UTR or no additional sequences (Empty), downstream to the Luciferase ORF. Cells were co-transfected with pRL-CMV Renilla. Values represent the ratio of Luciferase to Renilla signals, expressed as fold change (n = 3). *p < 0.05, one-way ANOVA. Error bars represent the mean ± SD.

(F) Western blot of PUM2, MFF and GAPDH (as loading control) in wild-type (WT) and ΔPBE-*Mff* C2C12 myoblasts, expressing either SCR or *Pum2*sh #1 (*Pum2*sh) shRNAs.
(G) Confocal imaging of SCR, *Pum2*sh #1, and *Pum2*sh #1 C2C12 cells. In some cells, *Mff* was knocked-down by small-interfering RNA (si*Mff*). Mitochondria are stained for TOM20 (green) and nuclei with DAPI (blue). Bottom, higher magnification of the mitochondrial networks. Scale bar = 10 μm. Quantification of the % of cells undergoing fission is shown in Figure S4I.
(H) Confocal imaging of ΔPBE-*Mff* myoblast cells transduced with SCR or *Pum2*sh #1 shRNA.
See also Figure S4.

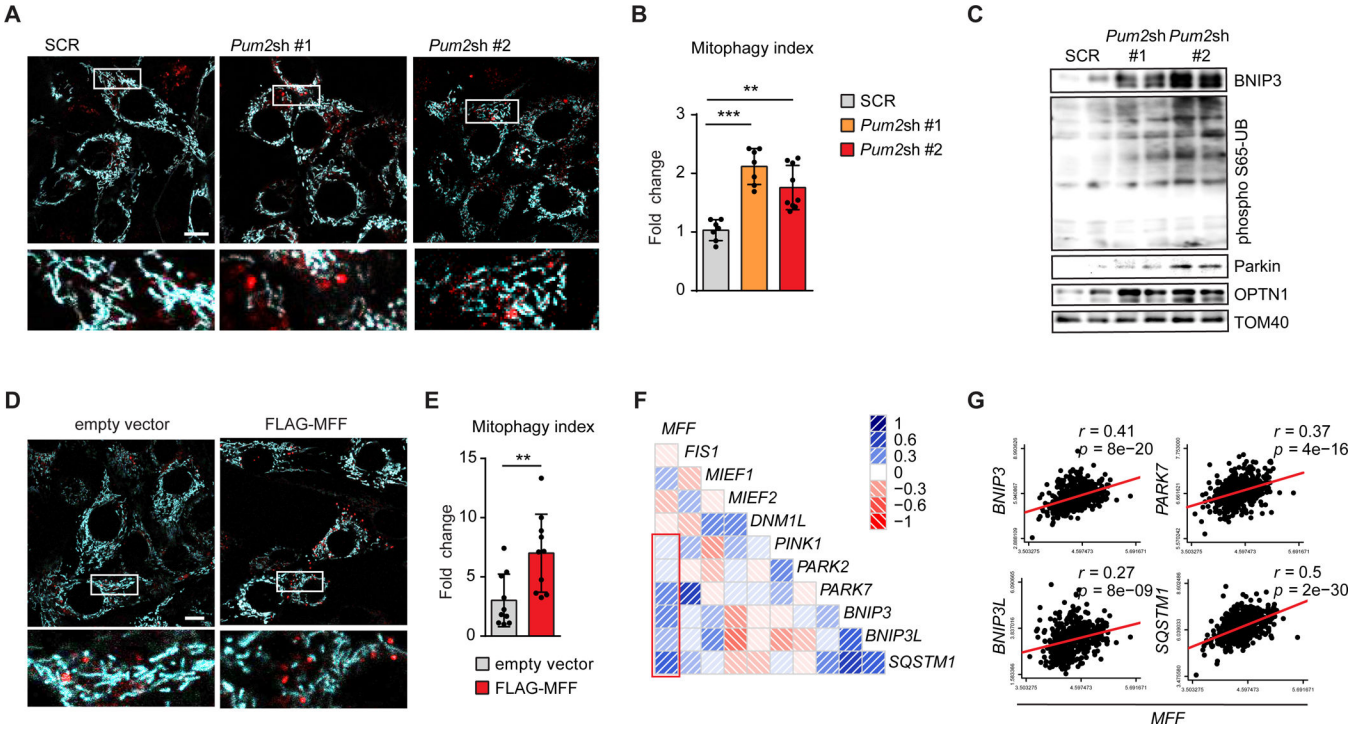

Figure 4. PUM2 regulates mitophagy via MFF.

(A) Representative images of C2C12 clones expressing SCR, *Pum2*sh #1 and *Pum2*sh #2 analysed with the m-KEIMA fluorophore. Scale bar = 10 μm.

(B) Quantification of the mitophagic rate from cells treated as in Figure 4A. **p < 0.01; ***p < 0.001, one-way ANOVA. Error bars represent the mean ± SD.

(C) Western blot of BNIP3, phospho S65 Ubiquitin, Parkin, Optineurin (OPTN1) and TOM40 (as loading control) in mitochondrial extracts of SCR, *Pum2*sh #1 and #2 C2C12 myoblasts (n = 2).

(D) Representative images of C2C12 myoblasts expressing either an empty vector or FLAG-MFF and stained with m-KEIMA.

(E) Quantification of the mitophagic rate of cells in Figure 4D. **p < 0.01, unpaired two-tailed Student's t test. Error bars represent the mean ± SD.

(F) Corrgram indicating Pearson's correlations amongst mitochondrial fission and mitophagy genes, from human muscle biopsies (GTEx). The red square highlights the correlations between MFF and mitophagy genes.

(G) Correlation analysis of mRNA expression levels of *MFF* and the mitophagy genes, *BNIP3*, *BNIP3L*, *PARK7* and *SQSTM1*, from Figure 4F.

See also Figure S5.

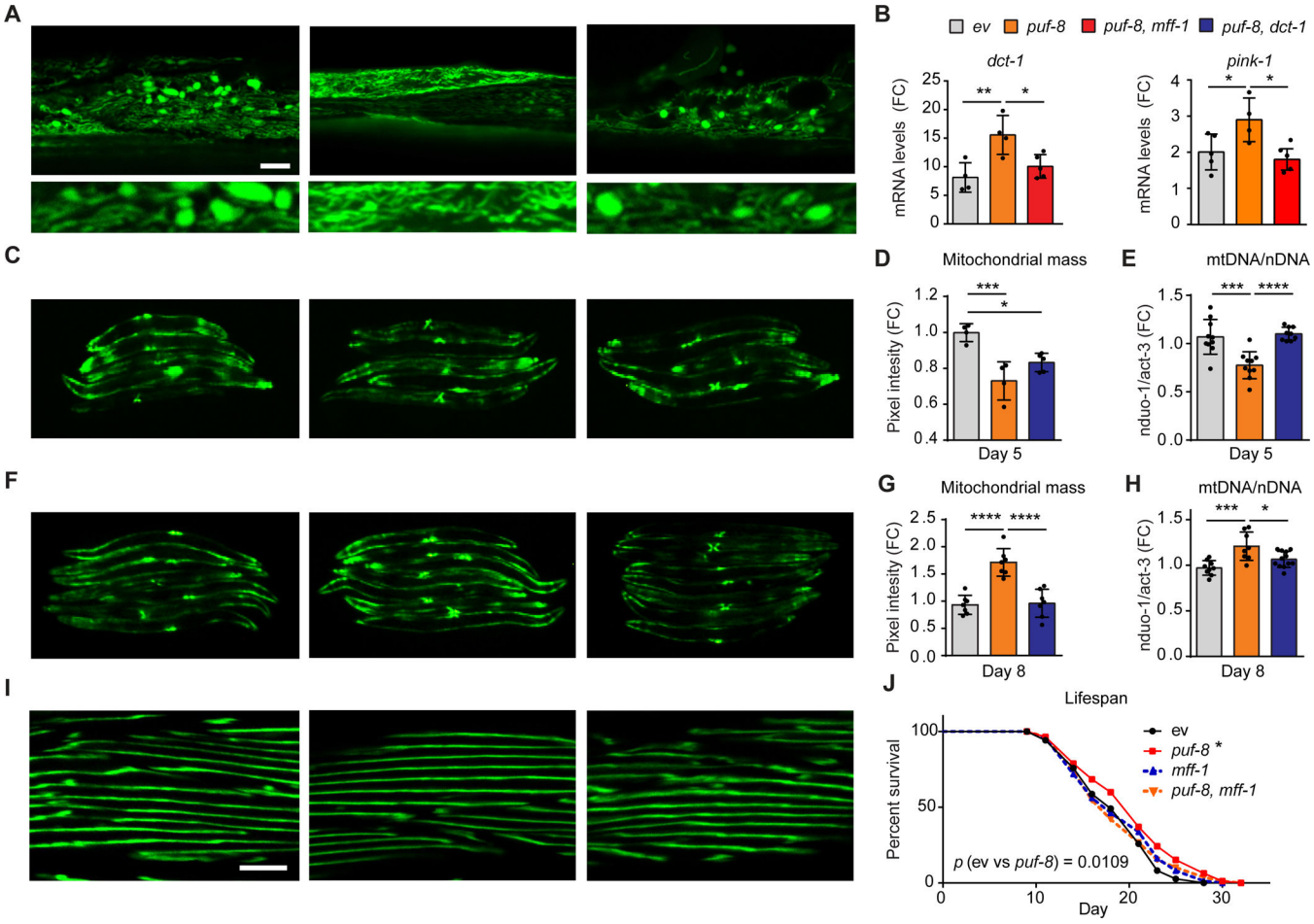

Figure 5. *puf-8* regulates mitochondrial fission and mitophagy *in vivo* in aged worms.

(A) Confocal imaging of worms expressing the muscle-specific p_{myo-3}::mito::GFP reporter to visualize mitochondrial morphology. Images compare old worms fed with either control (Day 8), *puf-8* or *puf-8*/*mff-1* RNAi. Bottom, higher magnification of the mitochondrial networks. Scale bar = 5 μm.

(B) q-RT-PCR of the mitophagy marker *dct-1* and *pink-1*, in *glp-1* worms treated as in Figure 4A ($n \geq 4$). *$p < 0.05$; **$p < 0.01$ one-way ANOVA. Error bars represent the mean ± SD.

(C, D) Imaging of p_{myo-3}::mito::GFP worms, at day 5, treated from day 1 with control RNAi, *puf-8* RNAi or both *puf-8* and *dct-1* RNAi (C). Corresponding quantification of the GFP signal ($n = 4$) *$p < 0.05$; ***$p < 0.001$, one-way ANOVA. Error bars represent the mean ± SD (D).

(E) Mitochondrial to nuclear DNA ratio (mtDNA/nDNA), using the *nduo-1* and *act-3* loci, respectively, of *glp-1* worms treated as in Figure 5C ($n = 7$). ***$p < 0.001$; ****$p < 0.0001$, one-way ANOVA. Error bars represent the mean ± SD.

(F, G) Imaging of p_{myo-3}::mito::GFP worms, at day 8, (F) fed from day 1 with RNAi as in Figure 5C and corresponding quantification of the GFP signal ($n = 7$) ****$p < 0.0001$, one-way ANOVA. Error bars represent the mean ± SD (G).

(H) mtDNA/nDNA ratio of Day 8 *glp-1* worms treated as in Figure 5F (n = 7). *p < 0.05; ***p < 0.001 one-way ANOVA. Error bars represent the mean ± SD.
(I) Confocal imaging of N2 worms expressing myo-3::GFP, to visualize muscle fibers, treated as in Figure 5A. Scale bar = 10 μm.
(J) Lifespan curves of *glp-1* worms fed with empty vector (ev), *puf-8, mff-1* of *puf-8/mff-1*, from day 1 of adulthood. *p < 0.05, log-rank (Mantel-Cox) test.
See also Figure S6.

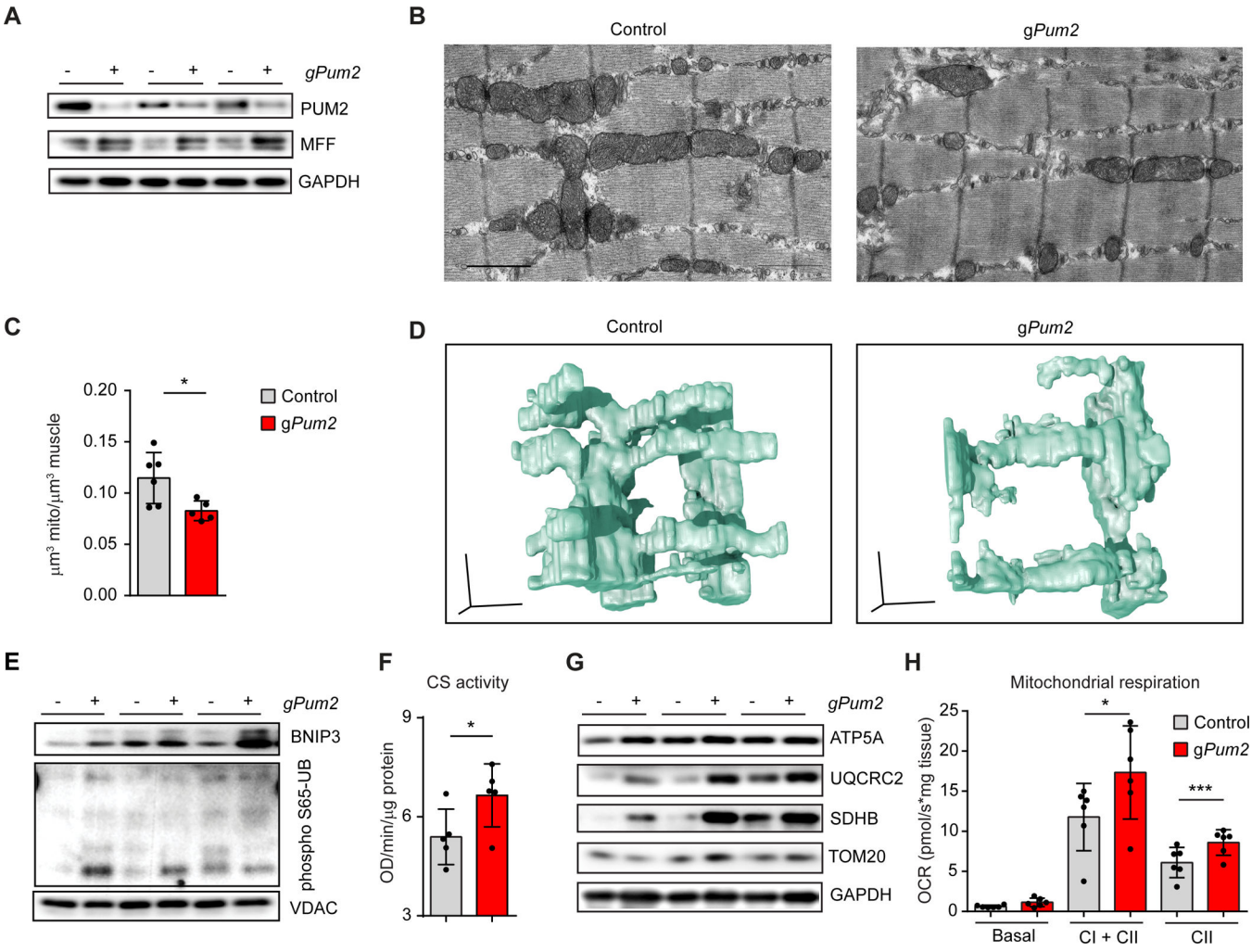

Figure 6. PUM2 regulates mitochondrial function in old mice.

(A) Western blot of PUM2 and MFF (GAPDH as loading control) in gastrocnemius muscles of old mice (24 months) injected either with AAV9s containing only Cas9 as control (−) or both Cas9 and a *Pum2*-targeting gRNA (+ g*Pum2*).

(B) Representative electron micrographs showing the morphology of intermyofibrillar (IFM) mitochondria of control and g*Pum2* mouse gastrocnemius muscles analysed by transmission electron microscopy. Scale bar = 1 µm.

(C and D) Mitochondrial volume quantification (n = 6) (C) and representative 3D reconstructions (D) of mitochondria from mice muscles as in Figure 5B. Scale bar = 0.5 µM. *p < 0.05, unpaired two-tailed Student's t test. Error bars represent the mean ± SD.

(E) Western blot of mitochondrial extracts from gastrocnemius tissues of mice as in Figure 5A. Membranes were probed against BNIP3, phospho S65 Ubiquitin and VDAC (as loading control).

(F and G) Citrate synthase (CS) activity (F) and western blot of the OXPHOS components ATP5A, UQCRC2 and SDHB and of TOM20 (GAPDH as loading control) (G) in gastrocnemius muscles as in Figure 5A. *p < 0.05, ratio paired Student's t test. Error bars represent the mean ± SD.

(H) Basal, State3_{ADP} (CI + CII)- and CII-driven mitochondrial respiration from gastrocnemius biopsies of mice treated as in Figure 5A. *$p < 0.05$; ***$p < 0.001$, ratio paired Student's t test. Error bars represent the mean ± SD.
See also Figures S7 and Movies S1 and S2.

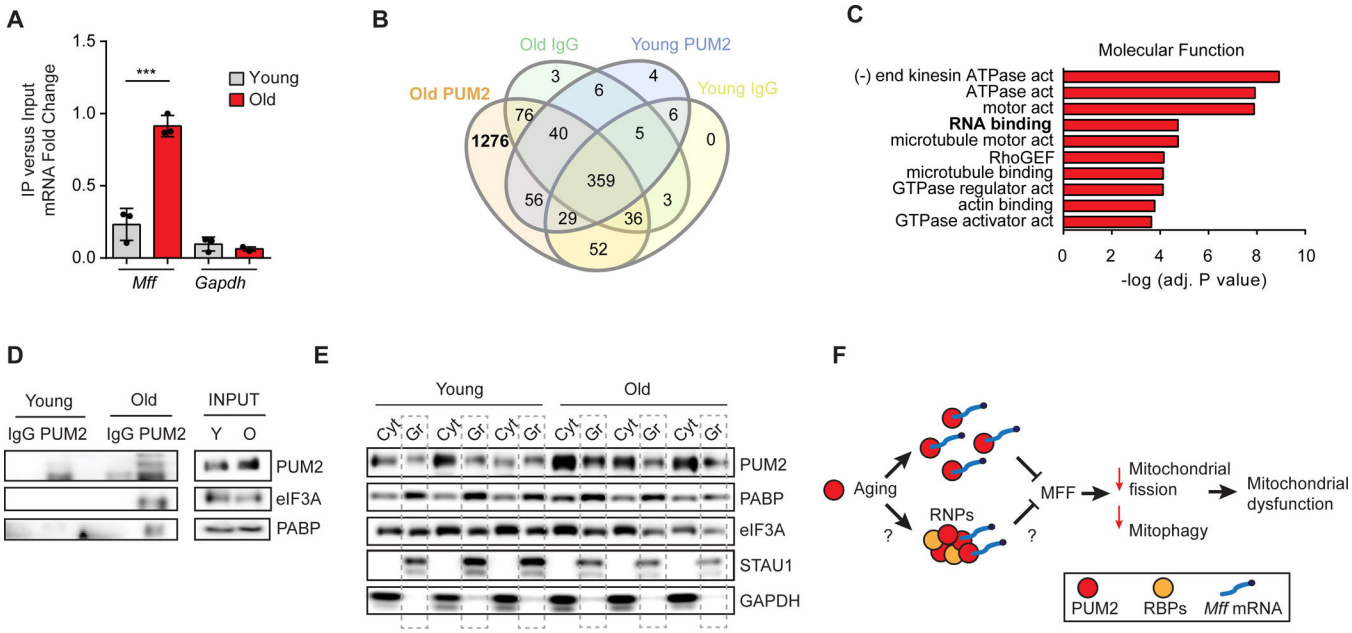

Figure 7. PUM2 binds *Mff* mRNA and is part of RNPs in old mice.

(A) q-RT-PCR of the indicated mRNAs bound to endogenous PUM2 from brain tissues of young (2 month) or old (24 month) C57BL/6J mice. ***p < 0.001, unpaired Student's t test. Error bars represent the mean ± SD.

(B) Venn diagram showing proteins bound to PUM2 or control IgG, in brainsfrom young or old mice, identified by LC-mass-spectrometry. The 1276 candidates interacting to PUM2 specifically in aged-tissues are highlighted in bold.

(C) Pathway enrichment analysis for the GO category, Molecular Function, of the 1276 proteins from Figure 7B (see also Figure S8B).

(D) Endogenous association of PUM2 to PABP and eIF3A in young or old brains. Tissues were lysed and immunoprecipitated with PUM2 or control (IgG) antibodies. Input = 1% of total lysate.

(E) Western blot of cytosolic and RNP-granule (Gr) fractions from brains of young or old mice (n = 3). Filters were stained with the RBPs, PUM2, PABP, eIF3A and STAU1. GAPDH confirms the purity of the RNP fractions.

(F) Schematic model of PUM2 impact on age-related proteostasis and mitochondrial function. PUM2 expression increases upon aging and this facilitates the capture/trapping of *Mff* mRNA, either alone (bottom) or in association with other RNA-binding proteins (RBPs; top) in RNP complexes. Consequently, PUM2 prevents *Mff* translation, impairing mitochondrial fission and mitophagy thereby leading to mitochondrial dysfunction.

See also Figure S8 and Supplementary Table 4.